The Effects of BMP2 on Bone Material and Mineral Characteristics in a Conditional Knockout Mouse Model

Bronwyn Stidley Bedrick
Washington University in St. Louis
Environmental Studies Program

Chapter 1 - Introduction

Introduction

Bones provide physiologically essential mechanical and chemical functions. Bone diseases, such as osteoporosis, and injuries are often debilitating, reducing mobility and quality of life. Understanding the complex processes of bone formation and maintenance is essential to the development of effective methods of treatment and prevention. While extensive research over the last hundred years has elucidated these mechanisms, many aspects still remain unexplained. Both the formation and maintenance of bone are governed by a variety of biochemical pathways that control the timing and nature of the formation of mineral within the body (biomineralization). Studies from a variety of fields, such as biochemistry, medicine, and material sciences, can help us address the causes, consequences, and cures of such diseases and the repair of injuries by examining the roles and relations of different aspects of these biological pathways. A common method employed to explore questions of bone disease involves suppression of a component of the pathway and examination of the consequences.

In this study, the expression of bone morphogenetic protein (BMP2), an essential protein involved in the growth and repair of bone, was suppressed in a conditional knockout mouse model. Mechanical and chemical tests were utilized to determine the consequences of this suppression on skeletal growth, with the goal to better understand how the protein affects bone structure and strength. Before the rationale for the study is laid out, background introduction on the materials and methods will be presented. First, a discussion of the composition and organization of bone will illustrate the complexity of bone as well as provide a foundation for a discussion of the process of bone formation, or ossification, along with changes in the bone with maturity and the bone's ability to prevent and repair fractures. Next, the mineral component of

bone will be explored, as its characteristics are a primary focus of this study. Then the selected analytical technique will be discussed. Raman spectroscopy offers an excellent means by which to measure the variability that occurs within bone and was used to determine whether the conditional knockout affected the chemical characteristics of the bone. Lastly, the rationale for this study will be presented.

Bone Composition

Bone composition reflects the specific functions of a given bone, and thus varies by age, body location, and species (Biltz and Pellegrino, 1969; Rogers and Zioupos, 1999). Strength and flexibility are the primary structural functions of bone—the scaffold of the body—and the composition of the bone determines how able it is to withstand loading and bending before its ultimate failure (i.e., fracture). The characteristics of bone owe their properties primarily to the presence and relative proportions of water, bone mineral, and protein. Mineral provides strength and stability to the bone, but results in brittleness, i.e., the bone will fracture with little plastic deformation (Penel et al., 1998; Launey et al., 2010). Brittleness can be detrimental during heavy loading or bending, resulting in fracture. The composition of this mineral is somewhat variable among bones. Type I collagen, non-collagenous proteins, and lipids comprise the bone organic component. Type I collagen, which makes up 85-90% of the total protein (Paschalis et al., 2001), allows bones to bend without fracturing but offers little mechanical support (Penel et al., 1998). Water, the smallest contributor (about 10% by weight) (Rogers and Zioupos, 1999), enables deformation as well, contributing to bone elasticity (Dunlop and Fratzel, 2010). Varying the relative proportions of these three components or their quality will affect the physical properties of bone. Exploitation of this variability has caused the evolution of specific bone materials to suit the needs of specific organisms (Figure 1.1). For example, the antlers of deer must be extremely

flexible during fights so as not to fracture. Deer antlers thus contain a low mineral-to-collagen ratio. The majority of mammalian bones maintain an intermediate ratio of mineral-to-collagen in order to maximize strength and flexibility while minimizing brittleness (Buckley et al., 2012). However, bone composition is not the only factor that affects the physical properties of bone. The interactions between the bone mineral and protein, as well as how the proteins interact with each other, affect the bone's ability to withstand load and to bend.

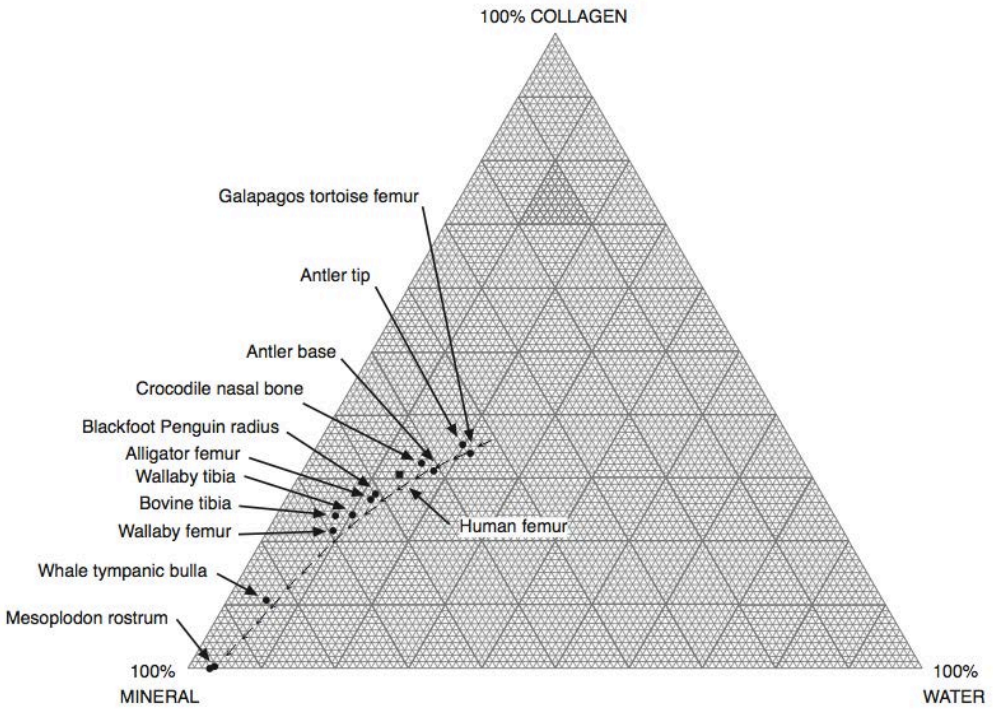

Figure 1.1: Ternary diagram showing the water, collagen, and mineral weight fractions of bone tissue. Bone tissues from eleven species are presented. The variability of these bones reflects the evolutionary adaptations of specific animals. Reproduced from Rogers and Zioupos, 1999, their Figure 1.

Bone Organization

Bone is a complex, hierarchical organ, as illustrated in Figure 1.2. Colloquially, the term bone is used to describe the individual structures of the skeleton. Each bone can be viewed as a

separate organ: a system that constantly remodels throughout life and provides a variety of mechanical and chemical functions for the organism.

At the tissue level, bone can be divided into two tissue types: compact tissue and cancellous tissue (Figure 1.2A). Cancellous bone tissue is primarily found in the medullary region containing bone marrow in the epiphyses, or the ends, of the long bone. Highly organized, this tissue resembles a sponge, from which its common name, spongy bone, derives. The small openings among the bone struts, or trabeculae, house a variety of cells and tissue as well as blood vessels (Glimcher, 2006). Compact bone tissue primarily constitutes the diaphysis, or the shaft, of long bones and ranges from several tenths of a millimeter to several millimeters in thickness. It consists of well organized, densely packed units called osteons (Glimcher, 2006; Launey et al., 2010). Osteons resemble cylinders with layers of bone material surrounding a blood vessel (Figure 1.2B and 1.2C). Thus, both types of bone tissue are highly vascularized.

At the cellular level, there are two primary types of cells: osteogenic cells and osteoclasts. Osteogenic cells consist of osteoblasts and osteocytes that help in the formation and maintenance of bone. Derivatives of mesenchyme, osteoblasts, remain at the surface of the bone in the exterior sheath, the periosteum, or in the interior cellular layer, the endosteum. On the surface of the bone, osteoblasts initiate the production of organic components of bone matrix as well as the production of new bone during growth and fracture repair, ultimately promoting the production of new mineral matrix into which they can be incorporated. When osteoblasts become fully incorporated into the mineral matrix (Figure 1.2C), their function changes, and they are called osteocytes. These cells are interconnected via channels containing fluid from the blood capillaries (Boskey, 2007). In addition, osteocytes are connected to the osteoblasts at the surface of the bone.

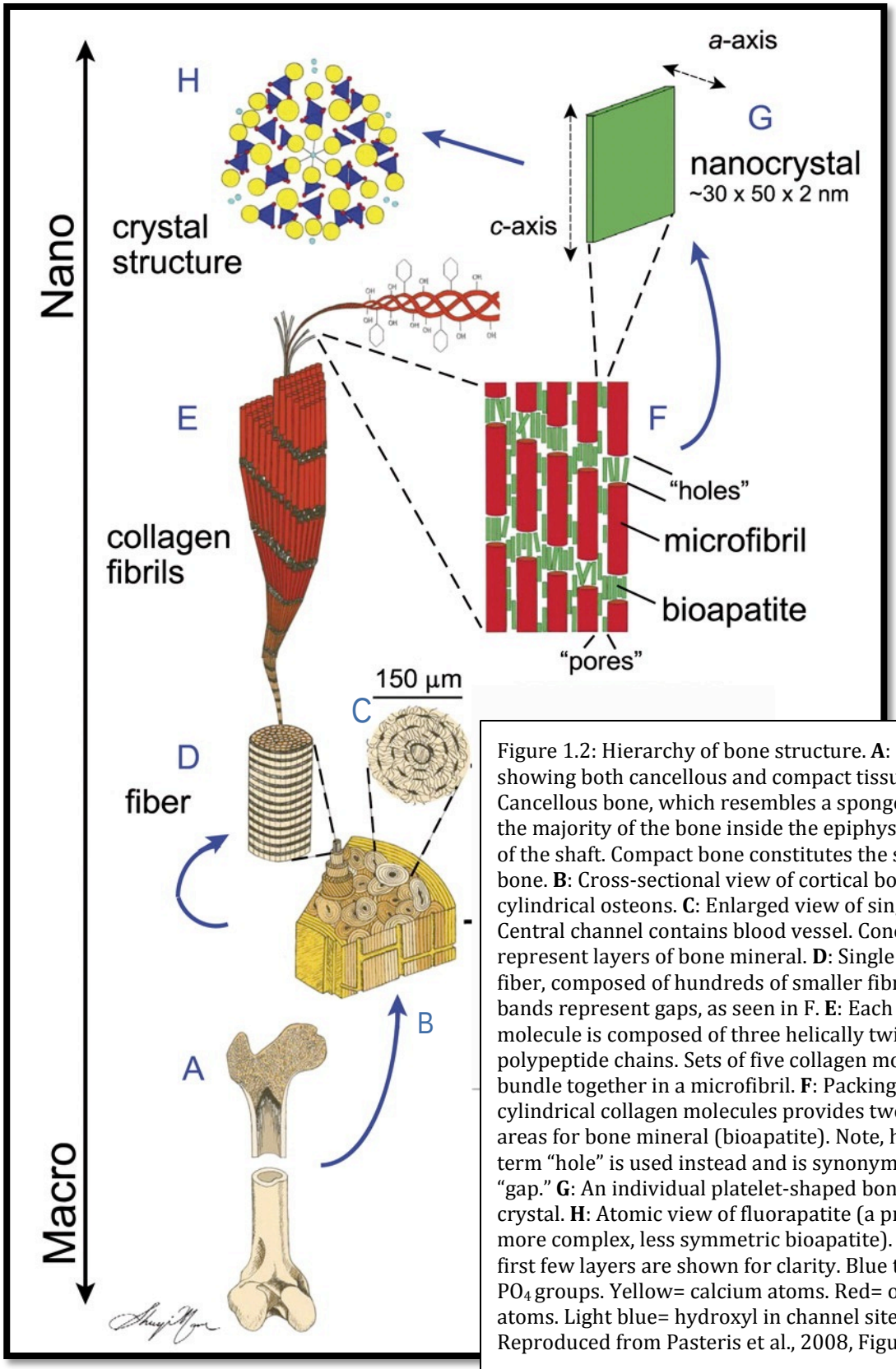

Figure 1.2: Hierarchy of bone structure. **A**: Long bone, showing both cancellous and compact tissue. Cancellous bone, which resembles a sponge, comprises the majority of the bone inside the epiphysis and some of the shaft. Compact bone constitutes the shell of the bone. **B**: Cross-sectional view of cortical bone, with cylindrical osteons. **C**: Enlarged view of singular osteon. Central channel contains blood vessel. Concentric lines represent layers of bone mineral. **D**: Single collagen fiber, composed of hundreds of smaller fibrils. Dark bands represent gaps, as seen in F. **E**: Each collagen molecule is composed of three helically twisted polypeptide chains. Sets of five collagen molecules bundle together in a microfibril. **F**: Packing of cylindrical collagen molecules provides two distinct areas for bone mineral (bioapatite). Note, here the term "hole" is used instead and is synonymous with "gap." **G**: An individual platelet-shaped bone mineral crystal. **H**: Atomic view of fluorapatite (a proxy for the more complex, less symmetric bioapatite). Only the first few layers are shown for clarity. Blue tetrahedral= PO_4 groups. Yellow= calcium atoms. Red= oxygen atoms. Light blue= hydroxyl in channel sites. Reproduced from Pasteris et al., 2008, Figure 2.

Unlike osteogenic cells, osteoclasts are derived from marrow stromal cells (Teitelbaun, 2000). They are responsible for the degeneration of bone matrix, which both initiates the necessary cellular remodeling of bone and liberates calcium ions functioning. Like osteoblasts, osteoclasts reside at the surface of the bone in order to easily receive signals to increase or decrease calcium ion excretion.

At the nanometer scale (Figure 1.2D-F), carbonated hydroxylapatite (CHAP), the mineral component of bone, and protein interact to form the structure of the bone organ and to enable its basic chemical and mechanical functions. The process of ossification shows how these two major components of bone relate to each other and their joint functions.

Bone Formation (Ossification)

Ossification (also called osteogenesis) occurs via two different cellular mechanisms: intramembranous ossification and endochondral ossification. The conversion of mesenchyme to osteoblasts that produce the organic matrix of bone is termed intramembranous ossification. This process occurs primarily in flat bones. Endochondral ossification describes the production of long bones from a cartilaginous precursor. Both processes are involved in the production of cancellous bone, which can be converted into compact bone (Cormack, 1998). During endochondral ossification, a bony matrix is formed, encasing the preexisting calcified cartilage. The interior cartilage is then digested, resulting in the formation of a hollow cavity (Marieb, 1997). Endochondral ossification primarily occurs at the epiphyses and thus governs a bone's length as well as its shape.

The formation of bone commences with the production of the organic matrix. Deposited in an extra-cellular environment by osteoblasts, this foundation is made of type I collagen. Collagen is the most abundant protein in humans, with type I collagen as the most prevalent

(Boskey, 2007). It can be viewed hierarchically, beginning at the finest scale. Three amino acids, i.e., glycine, proline, and hydroxyproline, constitute a polypeptide chain, each of which twists into a left-handed helix. The amine group of one amino acid and the carboxyl group of another amino acid are linked via a dehydration reaction. As a consequence, each polypeptide chain has an end with an unbound amine group (the N-terminal) and an end with an unbound carboxyl group (the C-terminal). A collagen molecule is composed of three of these polypeptide chains woven together, forming a left-handed helix. In turn, these collagen molecules are twisted together in a right-handed configuration, stabilized by hydrogen bonding. This hydrogen bonding is key to the ability of both the collagen molecule and bone to dissipate energy (Launey et al., 2010). Five collagen molecules packed together in a specific staggered array constitute a microfibril (Orgel et al., 2005). Hundreds of these microfibrils pack together to form a collagen fiber (Figure 1.2D and 1.2E). Cross-links between collagen fibers offer stability and ultimately provide the bone with mechanical strength and viscoelasticity.

There are seven major types of cross-links in type 1 collagen. Three of these seven are reducible, meaning that under certain conditions, the chemical nature of the bond can be changed, weakened, or broken. The other four are nonreducible (Paschalis et al., 2004). In addition to providing tensile strength and viscoelasticity (Paschalis et al., 2004), the characteristics of these bonds affect ossification significantly. For example, cross-linking patterns may affect nucleation of CHAP. Yamauchi et al. (1993) found that there tended to be a remarkable scarcity of cross-links between the N-termini in mineralized turkey tendon, where mineralization may first occur. Such low abundance of cross-linking was not found in soft-tissue collagen, suggesting that the presence of N-terminal amino acids may play a role in regulating the deposition of mineral. Differences in bone turnover and prevalence of cross-link formation in cortical and cancellous

bone tissue may help explain the mechanical differences between these two tissue types (Saito, 2009). Paschalis et al. (2004) found that the ratio between reducible and nonreducible cross-links differed among groups of: (1) normal premenopausal women; (2) postmenopausal women with bone fragility; and (3) men with bone fragility. Bone mineral density, however, did not vary significantly between the groups. Therefore, the properties of cross-linking must play an important role in how bone forms and functions.

The arrangement of collagen molecules dictates where mineralization can occur and differs for bones of varying degrees of mineralization (Buckley et al., 2012). The C-termini of the collagen molecules are separated from the N-termini of another, leaving a gap (Figure 1.2F). Each collagen molecule is staggered approximately one quarter of its length with respect to the other collagen molecules in the microfibril. The staggering of the molecules is such that the gaps

Figure 1.3: Two representations of gap channels formed between collagen molecules that provide a location for CHAP.
A: Based on the Hodge-Petruska Model, with straight rod collagen molecules. Note, here the term "hole" is used instead and is synonymous with "gap." (From Glimcher 2006, their Figure 16.)
B: Based on the work of Orgel et al. with right-hand helical twist. (From Alexander et al., 2012, their Figure 1.)

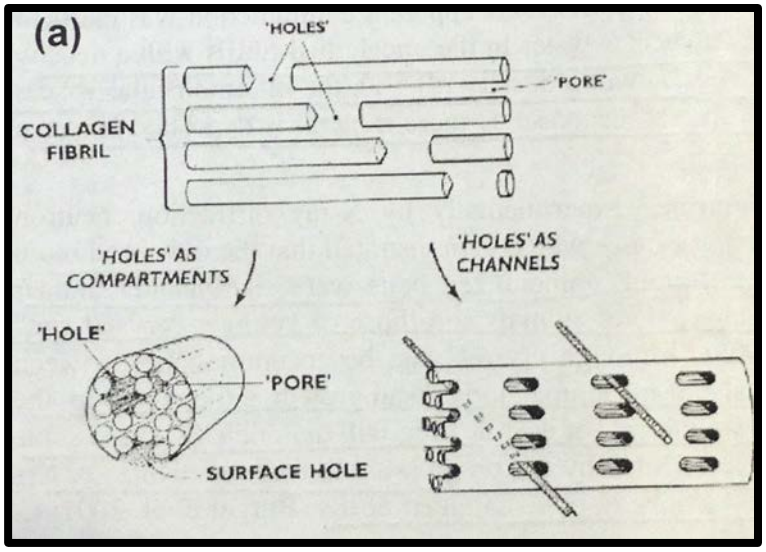

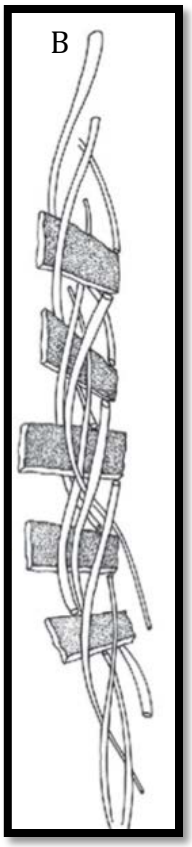

are not side-by-side but rather are offset, much like the stacking of bricks in a wall. In addition to this staggering, the microfibrils interdigitate in such a manner as to form a continuous fiber. In the quasihexagonally packed molecules of a microfibril, a channel of these gaps (Figure 1.3) is created (Orgel et al., 2006). According to classical thought, these gap channels are the location of the initial precipitation of CHAP out of extracellular fluids. At later stages of ossification, the crystallization occurs not only in these channels but also between the long axes of the collagen fibrils or "pores." The rationale behind this model is that these gap channels contain a large enough volume for individual crystallites to precipitate. According to this model, the pores in unmineralized collagen matrices are too small to accommodate individual mineral crystals. The volume of the gap channels, however, is not large enough to account for the total mineral present in bone. Therefore mineralization does occur in the collagen pores, and the precipitation of mineral crystals deforms the collagen matrix (Glimcher, 2006; Boskey, 2007; Nudelman et al., 2010).

Extracellular fluid is saturated with respect to the bone mineral (Pasteris et al., 2008). If there are no restraints on CHAP precipitation, biomineralization could occur ectopically throughout the entire body. Instead individual biomolecules, such as Bone Sialoprotein (BSP) and Osteopontin (OSP), can either inhibit or promote nucleation and growth of CHAP (George and Veis, 2008). These controls dictate where ossification occurs on a macroscale level (inhibiting ossification of tendons and ligaments) as well as on the nanoscale level (within the fibril). In addition, characteristics of the collagen fibrils themselves have been implicated in nucleation control. Nudelman et al. (2010) found that nucleation inhibitors stabilize amorphous carbonated phosphate (ACP), allowing it to enter the fibers before nucleation. Once the ACP is

inside the matrix, charged amino acid residues on the collagen fibrils provide an electrostatically favorable location for nucleation to occur.

The presence of ACP in developing and mature bone has been noted for decades (Glimcher, 2006). However, its presence and role are not well understood and the role is highly contested. It has been proposed that while this gel-like substance lacks crystallinity, its short-range order may make it an excellent precursor to mineral precipitation within bone. After this amorphous material has infiltrated the collagenous matrix, heterogeneous nucleation of another phosphate phase, octacalcium phosphate, can occur. CHAP can then form after hydrolysis of this intermediate phase (Mahamid et al., 2010). Because octacalcium phosphate has a similar structure to CHAP, heterogeneous nucleation on its surface will be energetically more favorable than single-stage homogeneous nucleation of CHAP. However, as explained by Glimcher (2006), the rapidity with which this process occurs makes witnessing the process *in vitro* difficult. Through use of cryo-SEM imaging and small- and wide-angle X-ray scattering, Mahamid et al. (2010) recently were able to document the presence of calcium phosphate globules in immature, actively forming bone (Figure 1.4). In addition, TEM images (Figure 1.5A) from Schwartz et al. (2013) of the transition zone between tendon and bone of a developing mouse tendon enthesis show unorganized mineralization consisting of dendritic mineral. More mature bone from the same area (Figure 1.5B) shows more alignment between the matrix and the mineral, suggesting the replacement or transformation of poorly organized to relatively well-ordered mineral-collagen composite.

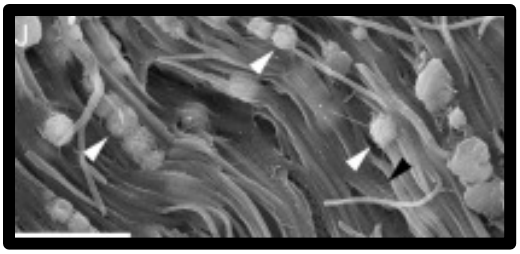

Figure 1.4: Cryo-SEM micrograph showing globules containing mineral levels of calcium and phosphate attaching to collagen fibrils. (From Mahamid et al., 2010, Figure 4.)

Alignment and organization within bone, especially in transition locations such as a tendon enthesis, can also be affected by loading and stress. For example, Schwartz et al. (2013) found that muscle loading at the shoulder rotator cuff in mice resulted in a higher degree of collagen organization and mineral crystallinity than was found in mice with induced paralysis. In addition, the carbonate concentration in the mineral component of bone was slightly higher in the paralyzed mice. Whereas there was no difference in the relative proportions of collagen and mineral between the two sets of mice, the mechanical properties differed significantly due to the differences in microscale collagen organization and mineral composition.

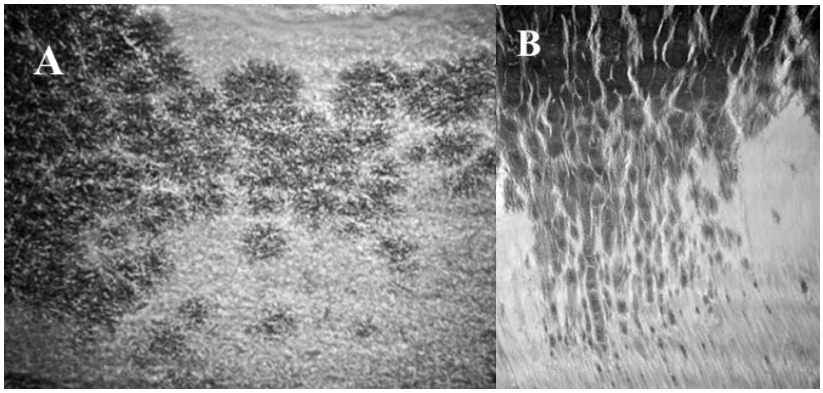

Figure 1.5: TEM images of the mineralization transition zone of the supraspinatus tendon enthesis. Dark regions represent mineral whereas light areas represent collagen.
A: Clusters of unorganized mineral in immature mouse (10 days). B: Mature (28 days) mouse bone shows more organization along collagen fibers.
(From Schwartz et al., 2012, Figure 6.)

The material properties of bone are due to the nature of its composition, and the interface between the mineral and matrix is integral to the unique set of properties of bone. In addition, from the extensive research on the effects of collagen on mineralization, we can see that in the composite, the characteristics of each component depend on those of the other. Therefore, one must be skeptical of studies in which the mineral and collagen have been separated through physical or chemical means, yet purport to reveal the inherent properties of collagen or mineral.

Changes in Bone with Maturity

Both the mineral and the matrix aspects of bone undergo significant changes with bone maturity. These changes impact the chemical, physical, and mechanical properties of the bone. During fetal development and early postnatal life, both the mineral and the organic matrix are poorly organized. The bone is termed "woven bone" during this period of immaturity. As the organism ages, these two components become more highly organized into osteon units. In addition, percent of mineralization and degree of mineral crystallinity increase with maturity (Akkus et al., 2004; Glimcher, 2006). An increase in crystallinity, or atomic order of a mineral, indicates that there is a longer length-scale of periodicity and organization of the atoms that constitute the crystal's lattice (Klein and Dutrow, 2007). While increasing mineralization in collagen-rich immature bones improves toughness, high bone mineral content, such as seen in the elderly, has been implicated in decreased ability to withstand stress (Currey et al., 1996.).

The composition of carbonated hydroxylapatite changes with maturity as well, altering its chemical and physical properties such as solubility. For example, calcium concentration increases with age (Glimcher, 2006). It is generally accepted that the CHAP crystals grow slightly with age. Some research indicates that while the crystals' size may increase, they are actually thinning in order to fit better into the smaller pores between the collagen fibers (Tong et al., 2002). However, the difficulty in measuring the parameters of the nanocrystals in bone raises questions about the accuracy of these measurements.

As mentioned above, bone maintains its viscoelasticity partly through cross-links between collagen molecules. Initially there is a positive correlation between an increase in cross-linking density and the maximum stress or load that can be withstood before deformation or fracture. The cross-links provide intermolecular traction that allows for greater yield but reduces

the molecules' ability to deform plastically. Therefore, at a certain cross-link density the molecules become almost brittle, resulting in fracture (Buehler, 2007). With age, the density of these cross-links increases, suggesting that brittleness in bones of the elderly may be explained partly by the increased levels of collagen cross-linking. In addition, with maturity there is an increase in the density of secondary, or smaller, osteons. These may be one of the greatest contributors to bone strength deterioration, as smaller osteons provide smaller crack bridges than larger osteons (Nalla et al., 2005). Crack bridges are uncracked regions along the crack length that reduce the propagation of a fracture, through absorbing energy (Launey et al., 2010). Therefore, as the bridges become smaller, the load absorbed decreases along with fracture inhibition. For the purpose of this study, it is important to recognize that mice do not have secondary osteons, and thus changes in bone strength with age are not due to increasing numbers of secondary osteons.

Fracture Prevention and Repair

In response to wear and use, bones will continually remodel and repair. Due to differential bone use, turnover rates vary by age, type, and location of the bone. Remodeling processes require reabsorption of both mineral and collagen and the subsequent precipitation of mineral on newly formed collagen (Glimcher, 2006). In addition to constant rejuvenation of bone material, there are additional intrinsic and extrinsic mechanisms that prevent fracture development and propagation. For example, small zones within the bone are allowed to fail so as to dissipate energy and prevent a larger fracture from forming (Launey et al., 2010). When a bone experiences a level of strain in which the energy cannot be dissipated or in which the fracture cannot be deflected, the bone will fracture. In normal healthy bones, a bony or cartilaginous callus will be produced in order to fuse the fragments of the broken bone. In

addition, dead bone will be absorbed (Cormack, 1998). However, in diseased or abnormal bone, callus formation and fracture repair may not occur (Tsuji et al., 2006; Chappuis et al., 2012).

Bone Mineral

Although bone mineral is frequently referred to as hydroxylapatite, the mineral component of bone differs significantly from geologic or synthetic hydroxylapatite. As seen above, the process of biomineralization is initiated and carried out by cellular processes, and the mineral crystallites are constantly dissolved and reprecipitated during remodeling. In addition, apatitic mineral found in bone tends to have significantly smaller, more rectangular platelet-like crystals (Daculsi et al., 1997) rather than the hexagonal prisms of geological apatite (Klein and Dutrow, 2007). CHAP crystals contain more vacancies and higher degrees of carbonate substitution than found in geologic hydroxylapatite (Boskey, 2007). The levels of carbonation in bone mineral range from 5 to 8 weight percent depending on animal species and specific bone (Penel et al., 1998). Most analyses of carbonate concentration in geologically occurring apatites have been carried out on igneous apatites that are formed at significantly higher temperatures (hundreds of degrees Celsius) than in biological processes. These analyses usually portray igneous apatites as containing effectively no carbonate. However, sedimentary phosphorites formed at ambient temperatures contain detectable levels (Skinner, 2005). For example, carbonate accounted for 6.04 weight percent of a South African francolite (carbonated fluorapatite) outcrop—these levels are comparable to those in bone (Deer et al., 1966).

Carbonated hydroxylapatite normally comprises 45-70 weight percent of bone (Roger and Ziopus, 1999). Its high concentration in bone is partly due to apatite's unique structure. Bone has significant physiological function beyond simply supplying structural support. Apatitic minerals can incorporate a wide range of ions into their structure, allowing bone to function as a

reservoir for biologically essential elements. For example, 80 weight percent of the body's phosphorus, 99 weight percent of the body's calcium, and 50 weight percent of its magnesium are stored in CHAP or on the surface of the crystals (Daculsi et al., 1997; Skinner 2005; Glimcher, 2006). Thus, a change or defect in the chemical make-up of bone mineral may affect more than structural characteristics; heart functioning, ATP and protein synthesis, blood clotting, and a number of other essential physiological processes depend upon the biological availability of these elements. The ability of the ions to be easily released into the blood stream or extracellular fluid results from the small volume and the large surface area of the crystals, on which ions bind (Glimcher, 2006). However, the ability to easily release atoms from its lattice coupled with the wide range of incorporable atoms may have physiological disadvantages as well. For example, lead can be incorporated into the apatitic lattice, essentially providing the body with a life-long supply of a toxic element gradually rereleased into the blood stream.

Crystalline structure

Within a crystal, ions surround one another in a systematic fashion. The geometry of the coordination, or how the ions arrange themselves in the crystal structure, depends primarily on the characteristics of the central ion. The coordination also depends on the physical environment (i.e., temperature, pH, and pressure) in which the crystal growth occurs. In general, a cation is surrounded by a specific number of anions governed by the need for charge neutrality and the relative size of the ions. For example, in phosphate, P^{5+} is surrounded by four O^{2-}, leaving the ionic group with a charge of -3. This four-fold coordination results in a $(PO_4)^{3-}$ tetrahedron. In the carbonate ion, the central carbon atom is surrounded by three oxygens, forming a $(CO_3)^{2-}$ triangle. These ionic groups may share one or more atoms with other groups to achieve charge neutrality. Groups then arrange themselves with respect to one another in order to reduce energy.

When a group is omitted, or replaced by another, the nature of the neighboring ionic group changes in response. In the case where charge is not conserved (e.g., omission of an ion or substitution involving unequal charges), substitution or omission of another ion or ionic group is necessary. Therefore, a change in one group in the lattice not only affects the bonds between it and its neighboring ions, the change impacts whether other groups of ions must be omitted or added. When substantial alterations occur within a lattice, the overall physical and chemical properties of the crystal can change. CHAP is an excellent example of how a mineral's properties vary with substitution.

Hydroxylapatite is one of the three end-members of the mineral group apatite. It is distinguished from the other end-members, fluorapatite and chlorapatite, by its incorporation of hydroxyl into the channel sites, resulting in the formula, $Ca_5(PO_4)_3OH$. Within this hexagonal crystal lattice system, calcium has either nine- or seven-fold coordination. Phosphate tetrahedra link to columns of the ninefold-coordinated calcium ions (Ca1). Channels formed within the lattice contain the sevenfold calcium ions (Ca2) as well as the hydroxyl groups (see Figure 1.6) (Ivanova et al., 2000). In general, the c-axes of the mineral align with the long axes of the collagen fibers in bone (Elliott, 2002; Boskey, 2007).

As a consequence of apatite's forgiving structure, many different ions and ionic groups can be incorporated into its structure. These substitutions significantly affect the chemical and physical properties of the mineral, especially solubility. The incorporation of these ions and ionic groups impact crystal growth as well. CHAP is usually represented as $Ca_{10-x}(PO_4)_{6-x}(CO_3)_x(OH)_{2-x,}$ and the elements most associated with hydroxylapatite substitution are fluoride, carbonate, sodium, and magnesium (Daculsi et al., 1997). Magnesium, as well as $(HPO_4)^{2-}$ groups, is found at the surface of the bone mineral, where it is not totally

included in the mineral lattice (Glimcher, 2006). Carbonate is the primary substituent in bone hydroxylapatite and can substitute in either or both of two sites in the hydroxylapatite lattice: the hydroxyl site (Type A) and the phosphate site (Type B) (Elliott, 1994; Glimcher, 2006). Type B substitution occurs at crystal formation temperatures between 50 and 100°C (Penel et al., 1998) and is a much more common substitution mechanism than Type A for CHAP in bone (Elliott, 1994; Daculsi et al., 1997). During Type B substitution, a coupled substitution occurs in order to maintain charge balance. While $(CO_3)^{2-}$ substitutes for $(PO_4)^{3-}$, Na^{+} replaces Ca^{2+} and vacancies in both the Ca^{2+} and OH^{-} sites arise so that $(CO_3)^{2-}$ may replace $(PO_4)^{3-}$. While the carbonate triangle might occupy any of the four phosphate tetrahedral faces, the triangles tend to occupy

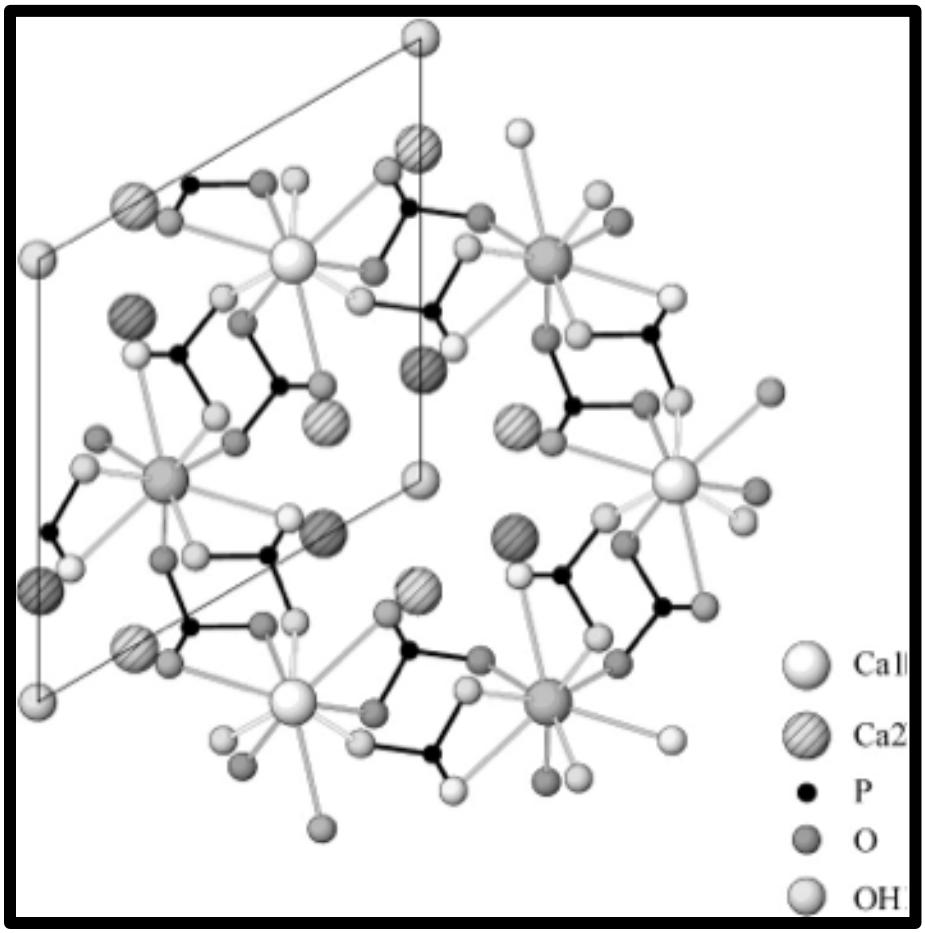

Figure 1.6: Crystal structure of hydroxylapatite. Ca1 refers to ninefold coordinated calcium ions and Ca2 refers to sevenfold coordinated calcium ions. (From Ivanona et al. (2000), Figure 1.)

the faces that align with the c-axis of the lattice (Ivanova et al., 2000). Unlike in Type B substitution, carbonate in Type A substitution replaces a smaller ion, $(OH)^-$. Therefore, more energy is required to overcome such an unfavorable substitution. The temperature at which this substitution is highly favored is much higher (several hundred to 1000°C) than in biological settings, making it a less favorable mechanism for substitution. And yet, Type A substitution is observed to account for 10-15 mole percent of carbonate in hydroxylapatite in bone (Elliott, 1994).

Carbonation affects the chemical and physical properties of the crystals. The carbonate group does not fit perfectly into either the phosphate or hydroxyl site. The distortion resulting from its inclusion results in localized microstrain, as the surrounding polyhedral bonds are distorted (Ivanova et al., 2000). As a consequence, bond energies and thus solubility increase (Baig et al., 1998). The increased solubility can also be explained by bond strengths; carbonate bonds are weaker than those in phosphate, thus increasing the mineral's solubility, especially in acid (Elliott, 2002). In addition, the crystal's size may be constrained (Pasteris et al., 2008), and the crystallinity reduced as carbonation increases (Daculsi et al., 1997; Glimcher, 2006). Carbonate distribution is determined not only during mineral precipitation, as the proportion of Type B carbonate increases with maturity (Akkus et al., 2004).

Technique (Raman and why it is useful)

There are many techniques used to analyze the structural and chemical characteristics of minerals, such as X-ray diffraction (to determine structure), electron-probe microanalysis (composition), and infrared and Raman spectroscopies (molecular-structural information). Each provides a different array of information. In this study, Raman spectroscopy was used to examine the molecular-structural characteristics of bone.

Raman spectroscopy uses monochromatic light to determine the vibrational behavior of covalent bonds in crystals through examining the behavior of scattered light. In the Laser Raman Microprobe, a laser of monochromatic visible light is generated and travels through an optical fiber. It is then focused through a microscope objective onto the sample on the microscope stage where the incoming photons from the laser interact with the material. The scattered photons either undergo a change in energy (inelastic/Raman scattering) or remain unchanged (elastic/Rayleigh scattering). A fraction of the incoming photons (1 in 10^7) scatter with a changed (typically lower) energy. The energy lost during the scattering process is a direct result of vibrational modes of the covalent bonds in the material, therefore reflecting both the bond energies and the symmetry of different compounds in the sample (Pasteris, 1996). For the majority of the time, the photons lose energy, and Stokes lines are produced. These lines or peaks are customarily measured using a Raman spectrometer (Wenk and Bulakh, 2004). When the photons gain energy, Anti-Stokes lines are produced.

There are many benefits to using Raman spectroscopy. This technique allows one to acquire point analyses rapidly and with good micrometer-scale spatial resolution, rather than an overall bulk analysis of a whole sample. Therefore Raman spectroscopy allows one to monitor differences across a mineral, such as point defects, or temporal crystallization composition that would be invisible in a bulk analysis. However, if the data collected is from a spot of contamination or is an anomaly, incorrect conclusions about the bulk composition may be made. Therefore any research design should involve multi-point analysis from the same sample so that erroneous conclusions about the bulk composition of the material are avoided. Unlike X-ray diffraction, which is classically used in crystal analysis, Raman spectroscopy can provide information about amorphous materials, such as ACP.

Spectra produced during Raman spectroscopy show intensity of the scattered photons versus the relative wavenumber. The relative wavenumber, or Raman shift, reflects the amount of frequency change between the incoming laser photons and the outgoing scattered photons. This change in frequency is equal to an energy that corresponds to a vibrational bond energy within the sample. Several parameters are monitored in the spectra, including the position, width, and area of individual peaks. The positions of the peaks identify the phase(s) in the sample, as well as specific molecular-structural components within a phase, for instance, phosphate and carbonate components in the CHAP of bone mineral. A strong peak at about 960 Δcm^{-1} represents the P-O stretching vibration for phosphate, and its exact position indicates that the phase is apatite. The full bandwidth of a peak measured at half-height indicates the degree of atomic order of the material and thus is one proxy for its crystallinity; the narrower the band, the greater the atomic order. Relative proportions of submicrometer phases and molecular components within each phase in the material are obtained through examining ratios of the areas of the pertinent peaks. For instance, Raman spectroscopy is a useful technique for evaluating the mineral-to-matrix ratio in the bone and the relative carbonate concentration within the mineral.

Rationale for Study (including issues with mice)

Bone morphogenetic protein (BMP) comprises a family of multi-functional growth factors responsible for the development of neurons, heart, cartilage, and bone (Chen et al., 2004; Lowery et al., 2011). Over-expression of BMPs may result in cancer and a variety of congenital diseases (Chen et al., 2003). Under-expression or deletion of a BMP gene often results in deleterious bone growth, ineffectual bone repair (Lowery et al., 2011; Mi et al., 2013; Chappuis et al., 2012; Tsuji et al., 2006), and nonviable fetuses (Chen et al., 2003). Exogenous BMPs are also used clinically in the treatment of bone diseases and for fracture repair. BMP2, which is the

focus of this study, plays an integral role in formation of bone through initiating the differentiation of the mesenchymal cells into osteoblasts and chondrocytes (Cheng et al., 2003; Mi et al., 2013, and references therein). Indeed, BMP2 may be one of the few bone morphogenetic proteins that can effectively induce differentiation from mesenchymal cells, whereas the majority can only induce ossification in mature osteoblasts, making BMP2 essential for fracture healing to occur (Chen et al., 2003; Tsuji et al., 2006). In addition, sufficient levels of BMP2 trigger callus cell differentiation and the formation of secondary ossification centers. Thus, BMP2 plays an important role in fracture repair as well as fracture prevention (Lowery et al., 2011; Chappuis et al., 2012).

As a consequence of its extensive impact on bone growth and repair, BMP2 could become the basis for treatment of a variety of bone injuries and diseases, such as osteoporosis (Turgeman et al., 2002). For example, treatment with BMP2 and recombinant human BMP2 (rhBMP2) has already proven to enhance the success of bone grafts (Murakami et. al, 2002; Chappuis et al., 2012), regeneration of amputated bone (Seeherman et al., 2004; Yu et al., 2012), treatment of fracture non-unions and spinal fusion (Chen et al., 2004; Hasharoni et al., 2005), in addition to accelerating fracture repair (Einhorn et al., 2003; Seeherman et al., 2004; Yu et al., 2012). Considerable research has been conducted on the role of BMP2 in bone formation and healing, but its role in differentiated cell function during growth remains uncertain.

In this study, the role of BMP2 expressed in osteogenic cells was investigated. The gene for BMP2 expression was suppressed (knocked out) in early stage osteoblasts. Early osteoblasts were targeted for several reasons: 1) BMP2 is strongly expressed in osteoblasts in the periosteal layer three days after loading (Wohl et al., 2009); 2) osteoblasts play critical roles in woven bone formation; and 3) the Osx-Cre with Green Fluorescent Protein (GFP) does not lose effectiveness

throughout an organism's life. Mechanical tests performed on the mice revealed significant differences in the material properties of the bone. The results from the mechanical tests suggested that the knockouts performed better or comparable to wildtype under normal loading conditions, but once trauma occurred, their bones failed more easily. The osteoblast knockouts developed malocclusions with varying severity in their front teeth, possibly decreasing their ability to eat and contributing to their smaller body size. However, mice heterozygous for the knockout did not have malocclusions, but were smaller in size (McBride, submitted). This suggests that the genetic modification impacts body size regardless of the presence of malocclusions. Smaller bone size could explain the significant mechanical differences seen between the wildtypes and knockouts. Therefore, to determine the cause of the mechanical and material differences, one must explore the alterations in the over-all bone size as well as the details of micro- and nano-scale constituents of the bone. In this study, Raman analysis was used to characterize the bone "composition" at several levels to determine if inherent material characteristics may be responsible for the observed mechanical differences and thus elucidate further the role of BMP2 in the body.

Chapter 2 - Methods

Mice

The bones analyzed by Raman spectroscopy in this study are part of a wider-ranging study led by Dr. Matthew Silva and Dr. Sara McBride of the Washington University in St. Louis School of Medicine. Their techniques for preparation of the mice along with my own technique for Raman analysis are described below.

Knockout (performed by Dr. McBride and colleagues)

The use of animals in this study was done in accordance with Washington University in St. Louis's IACUC approved protocols. Mice lacking BMP2 are nonviable and die *in utero* due to abnormal heart development (Chen et al., 2004). Performing a conditional knockout, however, avoids lethality. In this study, Cre-Lox recombination was used to target early-stage osteoblasts. During Cre-Lox recombination, the enzyme Cre recombinase is used to recombine targeted DNA sites (*loxP* sites), allowing one to perform conditional knockouts (Nagy, 2000). Sandwiching specific DNA segments between *loxP* sites is termed "floxing." Transgenic mice with the *BMP2* gene floxed (obtained through materials transfer agreement with Harvard University) were crossed with osterix-promoted Cre (Osx-Cre, B6.Cg-Tg(Sp7-tTA,tetO-EGFP/Cre)1Amc/J). *BMP2* deletion in the Osx-Cre mice affected mature osteoblasts and osteocytes, which differentiate from the targeted early-stage osteoblasts. Mice that are Osx-Cre conditional knockouts will be referred to as Osx-Cre cKO. Control (wildtype, WT) mice were littermates with both alleles floxed but without Cre. Osterix-promoted Cre has negative effects on mass and bone thickness unrelated to the knockout. By 12 weeks, the issues have been alleviated. Therefore, the youngest group of mice used was 12 weeks old. This 12-week cohort of 11 mice

and an additional cohort of 11 24-week-old mice were the primary focus of this study. Femora and humeri were analyzed for the 12-week-old cohort and the 24-week-old cohort, respectively.

Two techniques were used to confirm the knockout condition. First, a Green Fluorescent Protein (GFP) tag was attached to the Cre protein in Osx-Cre mice, producing green cells in which the protein was expressed at the time of tissue harvest. The GFP was not present in WT mice. Since the bones were not fixed, GFP most likely degraded quickly, and thus would not impact Raman spectra significantly. Secondly, immunostaining with BMP2 antibody was used to verify that BMP2 was not expressed in target cells. In addition, fluorochrome labels, Calcein Green and Alizarin Red, were administered to some mice shortly before death to mark new bone formation.

Structural and Mechanical Characteristics of Bone (performed by Dr. McBride and colleagues)

A variety of structural and mechanical tests were performed on bones from WT and cKO mice at 12 and 24 weeks. Dual X-ray absorptiometry was used to assess the whole body mineral content (BMC) and areal bone mineral density (aBMD). MicroCT was used to determine the characteristics (including tissue density, bone volume, and trabecular number) of cortical and cancellous bone tissue of the left tibia. In addition, three-point bending was performed on femora from both cohorts of Osx-Cre mice and provided information about ultimate force, post-yield displacement, stiffness, and energy to fracture. The humeri used for the Raman analysis did not undergo mechanical testing, but femora from the same mice did.

Bone Preparation (my methods)

The specimens were wrapped in gauze soaked in phosphate buffered saline (PBS) and stored at -4°C. The articulating ends of the humeri were removed and the samples were centrifuged to remove marrow. The femora specimens, which had undergone three-point bending,

had jagged edges from fracturing. To obtain even surfaces, and thus facilitate the acquisition of Raman spectra, the ends were smoothed using an Isomet saw **(**Buehler, Lake Bluff, IL**).** In addition, the femora were centrifuged at 12,000 rpm. For both bone types, if organic material such as blood or bone marrow remained visible, the specimen was rinsed with PBS. If a specimen was highly fluorescent under the Raman laser beam, the specimen was soaked in PBS and dried. New Raman spectra were then collected. Therefore, the spectra obtained and interpreted in this study had low fluorescence overall. Bones were mounted and stabilized in a soft yet firm material (packing peanut) so that the cross section could be analyzed (see Figure 2.1).

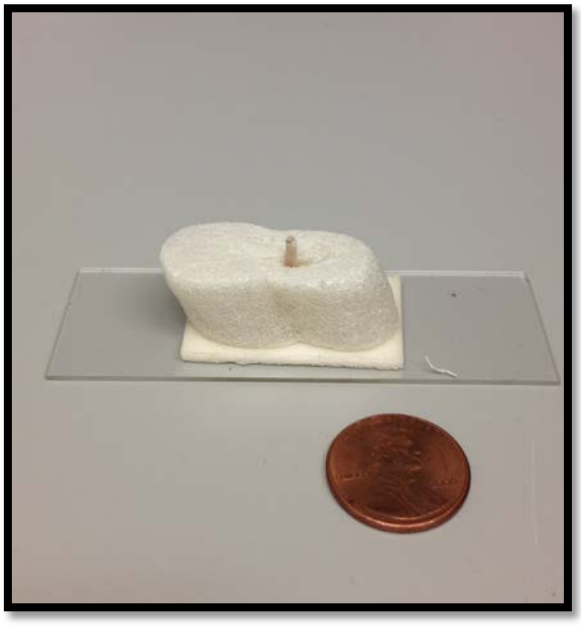

Figure 2.1: Set-up of mouse bone with penny for size comparison.

Comparison Bone

The ulna of a mouse from a different laboratory in England was used as a comparison for the femora and humeri WT and cKO bones. The preparation technique of the ulna is unknown. The cross section of the ulna was analyzed under the same conditions as the WT and cKO mouse bones. Unlike the humeri and femora, the ulna was not preserved in PBS and frozen, but was

stored at room temperature. Therefore the bone contained a lower moisture content than the femora and humeri samples.

Raman Spectroscopy

Acquisition of Spectra

Spectra were collected using a HoloLab Series 5000 Raman microprobe (Kaiser Optical Systems Inc., Ann Arbor). A laser of 532 nm excitation operated at 10 mW power (delivered to the sample surface) was focused by an 80x objective lens (N.A. = 0.75) to a beam spot of approximately 1 µm diameter. This wavelength provides excellent signal-to-noise but may introduce high fluorescent backgrounds if a sample contains blood or certain types of organic matter. However, high fluorescent backgrounds were not generally an issue for this study due to the specimen preparation technique. A 2048-channel CCD detector monitored signal in the

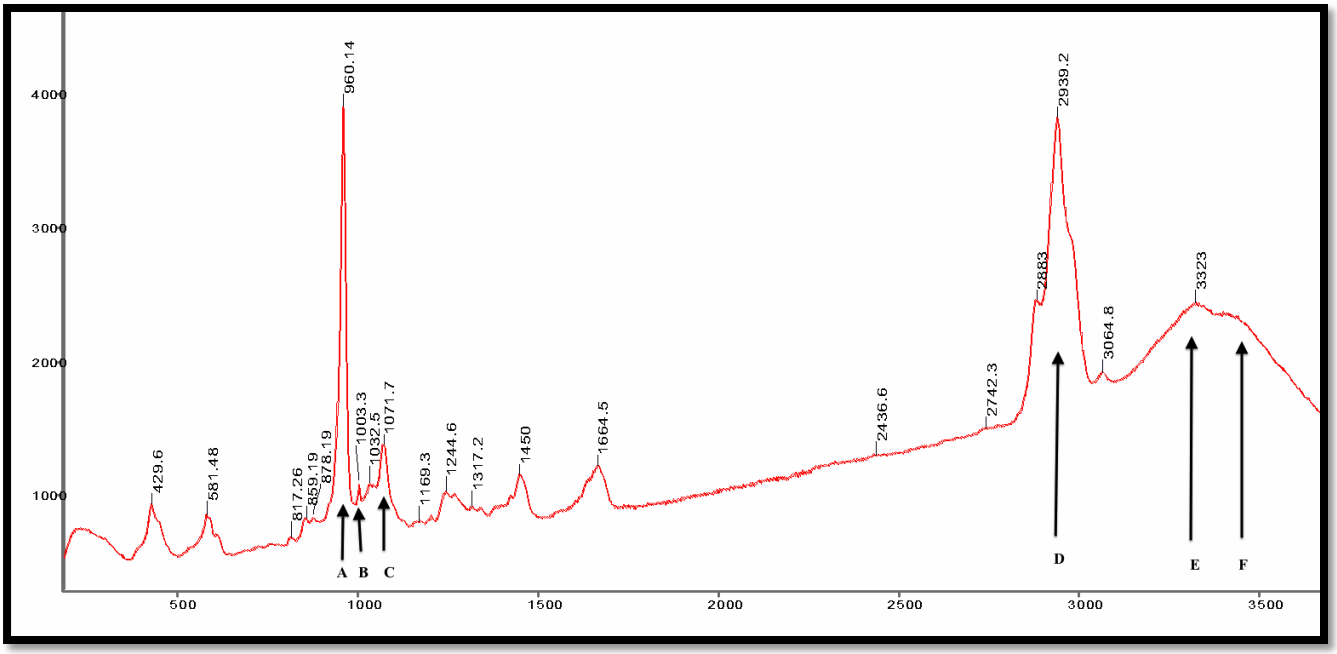

Figure 2.2: Typical Raman spectrum of mouse bone (inner edge of cortex) from 250 to 3600 Δcm^{-1}. Sample number: 6018 (WT). Wavenumber (Δcm^{-1}) of each major peak is displayed. Labels denote peaks of interest. Peak A: Phosphate-v_1 band (P-O symmetric stretch); Peak B: aromatic ring of phenylalanine (indicative of collagen); Peak C: Type B carbonation in CHAP; Peak D: C-H stretch; Peak E: N-H (amine); Peak F: O-H (water). Note: The intensity of the peak for Type A carbonation is relatively small and cannot be separated from adjacent peaks at this scale.

spectral range 100-4300 Δcm^{-1}. Each spectrum analyzed represents the average of 32 4-second acquisitions. A typical Raman spectrum of a mouse bone is presented in Figure 2.2. The chemical species and wavenumber corresponding to each peak of interest are presented in Table 2.1.

Chemical Species	Wavenumber (Δ cm^{-1})
Phosphate (ACP)*	950
Phosphate-v_1 band (P-O symmetric stretch)	960
Aromatic ring of phenylalanine (indicative of collagen)	1003
Type B Carbonation in CHAP	1070
Type A Carbonation in CHAP	~ 1100
Amide region	1200-1700
Unknown	2845
C-H stretch	2940
N-H (amine)	3316
O-H (water)	3340

Table 2.1: Chemical species and their spectroscopic positions.
Values from Frushour and Koenig, 1975; Penel et al., 1998.
*Note: there is not general consensus that the chemical species associated with the peak at 950 Δ cm^{-1} is ACP or an additional v-1 band of less well crystalline hydroxylapatite.

Spectra were collected from different regions within the bone to determine whether bone material varied by cortical region and to avoid making erroneous conclusions about the bulk composition of the material.

Within the 24-week-old cohort, there were 6 WT and 5 Osx-Cre cKO mice. Both right and left humeri of male and female mice were used for the Raman spectroscopic analysis. However, one bone was mislabeled during the analysis, and the correct body side could not be

determined. This mouse was excluded from analyses comparing the effect of body side, but was included for the remaining analyses. Six spectra were collected for each specimen: two near the inner edge of the cortex, two in the middle of the cortex, and two near the outer edge of the cortex (Figure 2.3). Spectra from the inner edge of the cortex tended to have high fluorescence, probably due to the proximity of this region to the marrow cavity. For two bones, only five spectra were collected due to high fluorescence, but the other spectra for these specimens were normal. Therefore, 130 spectra were collected for the 24-week-old cohort.

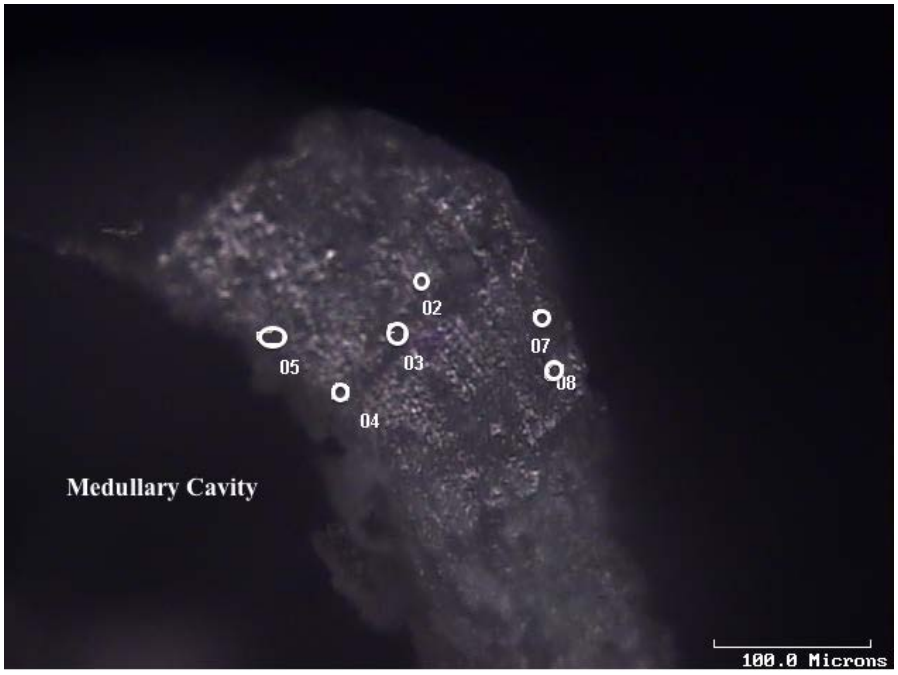

Figure 2.3: Microscopic image (20x objective) of the cross section of a right mouse humerus. Circles with accompanying numbers represent positions of Raman analysis. Middle cortex: 02, 03; inner edge of cortex: 04, 05; and outer edge of cortex: 07, 08. Sample number: 6011 (cKO).

The 12-week-old cohort (N=11) contained only males. In this cohort, 7 were WT and 4 were Osx-Cre cKO. Either the left or the right femora of these mice were used for Raman spectroscopic analysis, but not both. Due to the high fluorescence of the inner cortex in the humeri samples, the inner cortical area was not examined in the femur samples. For these mice,

only four spectra were collected for each specimen: two in the middle of the cortex and two near the outer edge. For one mouse, a spectrum was not collected near the outer edge of the cortex due to an extremely high fluorescence background, but the other three spectra for this specimen were normal. Therefore, there were 43 spectra collected for this cohort.

Four spectra were collected from the unrelated ulna sample: two in the middle cortex and two in the outer cortex. Before the acquisition of each spectrum, the bone was exposed to the laser for approximately ten minutes to reduce fluorescence. However, these spectra still had considerably higher background than those from the humeri and femora, which probably resulted from insufficient rinsing with PBS during the bone's initial collection (procedure unknown).

Spectra of insoluble type I collagen from a bovine Achilles tendon (Sigma Aldrich) and from a standard hydroxylapatite powder (Sigma Aldrich) were collected for comparison. Five spectra were collected from the type I collagen. One spectrum was collected for the hydroxylapatite standard. For all six spectra, the laser was focused by a 50x objective lens (N.A. = 0.55). Each spectrum analyzed represents the average of 32 4-second acquisitions.

Calcein Green and Alizarin Red were used to mark the formation of new bone in some mice. To determine whether these fluorochrome labels interfered with spectral measurements, spectra of Calcein Green solution and powder and Alizarin Red solution were collected. The Calcein powder had high fluorescence and overpowered the detector, so the laser's incident intensity was effectively reduced by lowering the magnification of the focusing objective. In this case, an objective lens of 5x (N.A. = 0.13) was used. One spectrum was collected for the powder and represents the average of 32 1-second acquisitions. The Calcein solution was placed on aluminum foil and one spectrum was collected. This spectrum represents the average of 100 50-millisecond acquisitions using a laser focused by a 20x objective lens (N.A.= 0.30). The Alizarin

Red solution was also placed on aluminum foil and one spectrum was collected using a laser focused by a 5x objective lens. This spectrum represents the average of 32 4-second acquisitions.

Raman Data Treatment

Grams32^{R} (Galactic Software, Inc., Salem, NH, USA) was used for all spectral processing. There were two regions of the spectra on which the analysis concentrated: the region between 700 and 1200 Δ cm^{-1} and the region from 2500 to 4000 Δcm^{-1}. The first region is characterized by the presence of $(PO_4)^{3-}$ and represents primarily CHAP. The second region is characterized by organic molecular-structural components and thus represents primarily collagen. Baseline correction was performed separately on each of these regions of the spectra. Performing this baseline correction brings down the fluorescence-elevated spectral region and flattens out the spectra so as to achieve more accurate band parameters and to make comparisons within and among spectra easier. In several cases, the background correction had to be extended beyond these spectral regions (i.e., to 4200 or 4300 Δcm^{-1}). Enlargement of the background-corrected region was performed to prevent the spectrally deconvolved bands from expanding past the area of analysis, and therefore to achieve greater accuracy in the band parameters. These spectra with the extended baseline corrections were deconvolved with the appropriate regional parameters.

Spectral peaks were deconvolved into their underlying bands of best fit using a mixed Gaussian-Lorentzian algorithm (see Figure 2.4 for an example of deconvolved peaks in the mineral region). During this process, the computer program determines the parameters of the bands. As a consequence, bands may be assigned arithmetically that do not have any physical reality (e.g., negative bands). Therefore, one can manually set limits on the bands to more accurately capture the features of the peaks. Restricting the parameters was required for a few bands. The starting width of four peaks was set lower than the program's default of 75

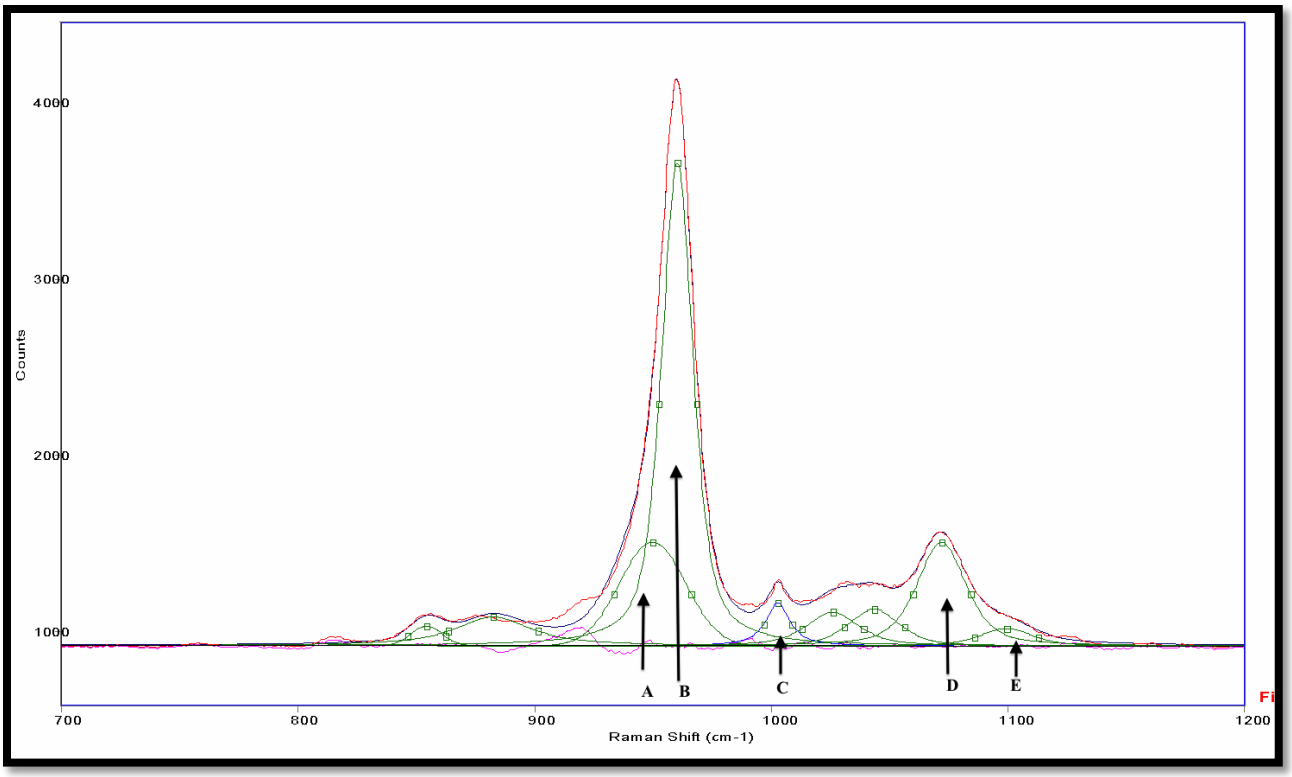

Figure 2.4: Background corrected and deconvolved Raman spectrum from 700 to 1200 Δcm^{-1} (mineral region). Sample number = 6018 (WT). Original trace (acquired spectrum) is in red. Added bands are in green. The residual, or the difference between the residual peak and the underlying band, is in pink. Labels denote peaks used in analysis. Peak A: Phosphate (ACP?); Peak B: Phosphate-v_1 band (P-O symmetric stretch); Peak C: aromatic ring of phenylalanine (indicative of collagen); Peak D: Type B carbonation in CHAP; Peak E: Type A carbonation in CHAP.

wavenumbers. The starting widths for the 1025 Δcm^{-1}, 1045 Δcm^{-1}, and the 3066 Δcm^{-1} bands were set to 20 wavenumbers, and the starting width of the 1003 Δcm^{-1} band was set to 10 wavenumbers. A maximum width was assigned to two bands to prevent the bands from overpowering adjacent bands and leading to false interpretations of bandwidths and areas. The maximum for the 1003 Δcm^{-1} band was set at 12 wavenumbers, and the maximum for the 3066 Δcm^{-1} was set at 80 wavenumbers. The starting and maximum widths were determined based on spectral peak characteristics and the fit of previously run deconvolutions.

Deconvolution was iterated 50 times for each run, and this process was repeated several times to fit the bands to the peaks more accurately and to accommodate adjustments should a band overpower or be overpowered by another. The Grams32^{R} software evaluates how well the sum of the bands represents the peaks by providing a correlation coefficient for the deconvolution. If the deconvolved spectra had an R^2 value greater than 0.999, it was considered adequate. There were 11 humeri spectra and 5 femora spectra that could not meet the 0.999 requirement. These spectra all had irregular aspects. For example, the collagen region for several of the spectra had abnormal shapes (see Figure 2.5 in comparison to the region between 2500-3500 Δ cm^{-1} in the normal spectrum in Figure 2.2) and bands could not be easily assigned to the peaks. The majority of these spectra were discarded for reasons presented later.

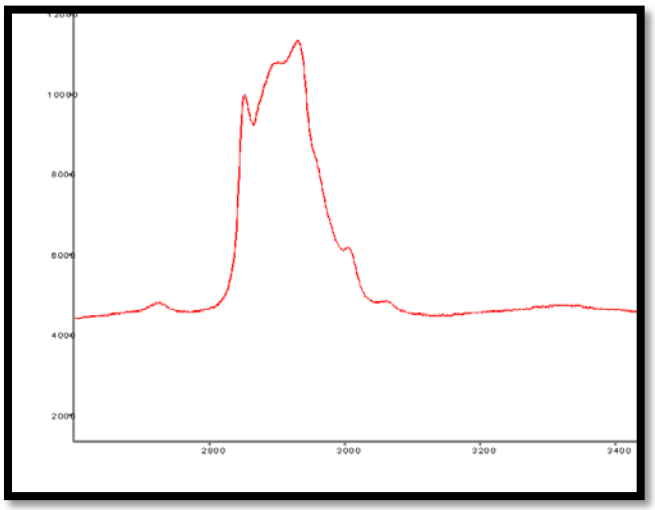

Figure 2.5: Example of spectrum with abnormal collagen region.

Raman Spectral Analysis

Each peak and its underlying bands can be described by a variety of spectral parameters. The positions of the peaks identify the phase(s) in the sample, as well as specific molecular-structural components within a phase (Table 2.1). Both band area and height (intensity) reflect the abundance of the species present in the 1 μm area analyzed under the microscope. The raw numbers of these parameters cannot be used to represent abundance alone, because they are impacted by a variety of factors, such as laser intensity on a given day and water content of a

sample. Instead, ratios are used to express the relative proportions of certain molecular-structural components. Fluorescence impacts the overall background, noise, and peak height, making height a less reliable representation of abundance than area (which is integrated peak height). Therefore, peak area ratios typically were used to express relative abundance. The full bandwidth of a peak measured at half-height indicates the degree of atomic order of the material and thus is a proxy for its crystallinity; the narrower the band, the greater the atomic order. Relative proportions of phases and molecular components of phases in the material irradiated during an individual analysis are obtained through examining ratios of the areas of the pertinent peaks. The mineral-to-matrix ratio (CHAP: collagen) for each spectrum was used to assess whether the mechanical characteristics seen in the cKO mice were a result of underlying material characteristics. In addition, the proportion of carbonate substitution within the CHAP was calculated to assess potential bone mineral abnormalities.

In assessing the mineral-to-matrix ratio, one of several collagen bands can be used as a matrix indicator. The 1003 Δcm^{-1} band represents a stretching vibration in the aromatic ring of phenylalanine and is unique to collagen. In contrast, the 2940 Δcm^{-1} band represents a non-specific C-H stretch that is found in substances other than collagen. In addition, a variety of amide bands (from 1200- 1700Δcm^{-1}) can be used in determining the mineral-to-matrix ratio. Whereas the 2940 Δcm^{-1} band is the strongest vibration in the organic phases, it is spectrally distant from the phosphate band (960 Δcm^{-1}). Using it as the indicator in a ratio of bands can make comparisons difficult, as the two bands that are being compared may have different intensities of background fluorescence. Such variations in relative background intensity can create artifacts in the band area ratios (Wopenka et al., 2008). However, this peak has been used for mineral-to-matrix ratios in numerous studies (e.g. Wang et al., 2013). Many studies have

successfully used amide bands in characterizing collagen and the mineral-to-matrix ratio (Paschalis et al., 2001; Paschalis et al., 2006; Nalla et al., 2006; Ager et al., 2006; Buckley et al., 2012; Inzana et al., 2012; Karampas et al., 2012). Whereas the amide bands are closer to the phosphate band than the 2940 Δcm^{-1} band is to the phosphate band, their poor signals in these spectra made them difficult to use. When comparing the relative proportions of collagen and mineral, the 1003 Δcm^{-1} band has the advantage of a consistently strong signal (although modest in intensity) and well-defined peak shape. It also is in close proximity to the 960 Δcm^{-1} band, ensuring that the background is approximately the same for both bands.

The identity of a peak at 950 Δcm^{-1} has been assigned to *v*-1 P-O stretch in amorphous carbonated phosphate (ACP) by several researchers (e.g., Kazanci et al., 2006). This peak may be viewed as an indicator for the degree of disorder in CHAP. Therefore, the relative proportion of mineral to collagen also can be described by using the area ratio of the sum of the areas of the 960 Δcm^{-1} and the 950 Δcm^{-1} bands to the area of the 1003 Δcm^{-1} band. In this study, the mineral-to-matrix ratio was calculated using several ratios (Table 2.2).

Carbonate substitutes in either of two sites in the hydroxylapatite lattice: the hydroxyl site (Type A) and phosphate site (Type B). Two different spectral peaks result from these two substitutions. A peak at about 1070 Δcm^{-1} represents carbonate substituted for phosphate (Type B), and a peak at about 1100 Δcm^{-1} represents carbonate substituted for hydroxyl (Penel et al., 1998). Five area ratios are used to determine characteristics of carbonation (Table 2.2). Total carbonate substitution is determined by the ratio of the sum of the areas of the 1070 Δcm^{-1} band and the 1100 Δcm^{-1} band to the 960 Δcm^{-1} band. The amount of Type B substitution is determined through the area ratio of the 1070 Δcm^{-1} band to the 960 Δcm^{-1} band. The sum of the areas of the 950 Δcm^{-1} band and the 960 Δcm^{-1} band may also be used in these ratios. The

proportion of Type B substitution to the total substitution is represented as the ratio of the area of the 1070 Δcm^{-1} band to the sum of the areas of the 1070 Δcm^{-1} and the 1100 Δcm^{-1} bands. These ratios are also described in Table 2.2.

Mineral-to-matrix	
Ratio 1	area960/area1003 P-O stretch/phenylalanine
Ratio 2	area960/area2940 P-O stretch/strongest C-H stretch
Ratio 3	(area950 + area960)/area1003 both P-O stretches/phenylalanine
Ratio 4	(area950 + area960)/area2940 both P-O stretches/strongest C-H stretch
Ratio 5	height960/height1003 P-O stretch/phenylalanine
Carbonation	
Ratio 6	area1070/area960 Type B carbonation/ P-O stretch
Ratio 7	area1070/(area950+area960) Type B carbonation/ both P-O stretches
Ratio 8	area1070/(area1070+area1100) Type B carbonation/ Total carbonation
Ratio 9	(area1070 + area1100)/area960 Total carbonation/ P-O stretch
Ratio 10	(area1070 + area1100)/(area950 + area960) Total carbonation/ both P-O stretches

Table 2.2: Ratios used in statistical analyses

Carbonate substitution in either location distorts the crystalline lattice and consequentially results in an increase in the width of the 960 Δcm^{-1} band, but not a change in the peak's position. Depending on the percent carbonation, the change in the width follows two separate models. Below 4% carbonation, the band broadens 0.90 Δcm^{-1} for every 1% increase in carbonation. Above 4%, the rate of broadening decreases to 0.10 Δcm^{-1} for every 1% increase in carbonation (deMul et al., 1988). The levels of carbonation in bone mineral range from 5 to 8 weight percent depending on animal species and specific bone (Penel et al., 1998). Carbonate substitution in CHAP in bone should then follow the latter model.

Statistical Analysis

There were fourteen primary study variables: ratios 1-10; peak position of 960 Δcm^{-1}, and the widths of 960 Δcm^{-1}, 1003 Δcm^{-1}, and 2940 Δcm^{-1}. Distributions of these variables were examined using boxplots by genotype (WT and cKO) and bone type (humeri, femora, and ulna). Multiple measurements were made on the same mouse, including measurements at three cortical locations (inner, middle, and outer) and both body sides (right and left) for the humeri and two cortical locations (middle and outer) for either the right or left femora. Measurements were made at two cortical locations (middle and outer) for the ulna. Potential differences among the cortical locations and the body side (right and left) were assessed utilizing boxplots and analysis of variance (ANOVA). The ANOVA models were used in a strictly descriptive manner since they did not incorporate the dependency among observations taken from the same animal. The median across all observations for an animal was used to summarize each variable, since the differences among these factors were not substantial or consistent. Utilizing the medians substantially lessened the effect of the occasional outliers. Other studies have similarly summarized multiple

observations for a bone, e.g., Akkus et al. (2004) used means to assess crystallinity and carbonation.

When an additional peak at 2845 Δcm^{-1} was observed, its effect on adjacent peaks in the organic region was assessed for those spectra. For variables whose values changed according to different deconvolutions (e.g., position 2940 Δcm^{-1}), differences in values between the two approaches were used. To assess whether the presence of this peak resulted from a change within the collagen framework, another collagen peak, 1003 Δcm^{-1}, was used for a comparison between spectra deconvolved with and without acknowledging the presence of this additional peak. Boxplots and ANOVA were used to assess differences, but since these ignored the dependency among observations within a mouse, these analyses were used in a descriptive fashion.

The primary focus of the analyses was to compare the fourteen study variables between the two genotypes and between the age cohorts. The medians obtained across all observations for a mouse were compared between the genotypes utilizing a two-sample t-test. All analyses were conducted separately by age-cohort (and thus bone type). Differences between the genotypes were summarized using the differences in the means and 95% confidence intervals. A similar approach was used to assess differences between the age cohorts by genotype. The measurements made on the ulna were summarized like those for the cKO and WT. Since only one specimen was analyzed, comparisons between the ulna and the other bone types were strictly descriptive and included an assessment of how different the ulna results were relative to the distributions for the humeri and femora. All statistical analyses were conducted in Statistical Analysis System (SAS, Version 9.3 for Windows; SAS Institute, Cary, NC, USA). The statistical analysis plan was determined under the guidance of Dr. Chris Stidley, a faculty biostatistician at the University of New Mexico, and was implemented with her assistance.

Chapter 3 - Results and Discussion

Multiple tests were performed on the conditional knockout mice and their wildtype controls to determine the role of *BMP2* in differentiated osteoblast function during growth. First, verification that the conditional knockout had the correct genotypic outcome was performed. Next, mechanical tests were conducted. The results of these tests shall be presented first since they were the impetus for my thesis project, which used Raman analysis to examine bone mineral and material differences between the genotypes.

Verification of Knockout and Phenotype Summary (performed by Dr. McBride and colleagues)

BMP2 was successfully knocked out in early stage osteoblasts and the Osx-Cre was expressed in the correct tissues. Knockout of *BMP2* in osteoblasts resulted in smaller mice. Specifically, Osx-Cre cKO mice showed a lower body weight and shorter tibia length at 12 and 24 weeks compared to control mice of the same age. Values for areal bone mineral density (aBMD), bone mineral content (BMC), bone volume, and total volume of cortical and cancellous tissues in Osx-Cre cKO were lower compared to those in control mice at 12 weeks. However, by 24 weeks, the differences were absent.

There were unexpected effects of the *BMP2* deletion that impacted tooth growth. All Osx-Cre mice developed malocclusions, which worsened with age and possibly decreased the mice's ability to eat. Malnourishment is a logical explanation for reduced body and bone size in these mice. However, there were no differences between the cKOs and the WTs in percent body fat, as would be expected in the case of malnourishment (Devlin et al., 2010). In addition, malocclusions were absent in heterozygous knockout mice that showed structure and strength outcomes that lay between the knockout and wildtype outcomes (McBride, submitted). Therefore,

any differences in the mineral properties between cKO and WT most likely result from *BMP2*'s effects on bone development rather than from malnutrition.

Mechanical Tests (performed by Dr. McBride and colleagues)

Osx-Cre cKO mice demonstrated altered material properties in their bones compared to their WT littermates. Forelimb strength was significantly reduced compared to WT at 12 and 24 weeks. However, ultimate stress, a size-normalized indicator for bone strength, was higher for Osx-Cre cKO than WT at 24 weeks. Bones from Osx-Cre cKO had a higher Young's modulus, suggesting that they were stiffer than WT bones. The observed lower post-yield displacement in the cKO bones indicated that they were also less ductile than normal bone. These size-independent properties demonstrated that Osx-Cre cKO bone material performed just as well or better than WT under normal loading conditions. However, once trauma occurred, the bone material failed, and the Osx-Cre cKO bones absorbed less energy than WT. These results indicate that *BMP2* expression in osteoblasts is important to post-natal bone growth and strength (McBride, submitted). Therefore, I investigated the chemical-structural properties in the Osx-Cre cohorts at 12 and 24 weeks. For the remaining text, "cKO" refers to Osx-Cre cKO unless specified otherwise.

Calcein Green and Alizarin Red Effects on Spectral Analysis

Raman spectra of both the liquid and powder form of Calcein Green (excitation at 495 nm and emission at 515 nm) showed no peaks within the CHAP or collagen regions of interest. The excitation wavelength (532 nm) of the Raman microprobe laser is sufficiently close to the excitation wavelength of the Calcein Green solution. Therefore, there was a high level of florescence when Calcein Green was examined under the Raman microprobe. However, since this compound is usually incorporated on a thin layer of periosteal or endosteal surfaces, it is

unlikely to significantly impact the areas investigated in the study (cortical bone). Spectra of Alizarin Red (excitation at 530-560 nm and emission at 624-645 nm also showed no peaks within the CHAP or collagen regions of interest. The excitation wavelength of the Raman microprobe laser is within the excitation range for this compound and thus there was a high level of florescence when it was examined under the Raman microprobe.

Molecular-Structural Differences

My thesis project involved Raman spectroscopy of bone samples from 12- week-old and 24-week-old cKO and WT mice. Analyses of the Raman spectra used the band position, width, and area values from the deconvolved portions of the spectra deemed most useful to the analysis, the mineral region (700-1200 Δcm^{-1}) and the collagen region (2500-4000 Δcm^{-1}). The ultimate goal of this project was to assess whether molecular-structural differences between cKO and WT mice could explain the mechanical differences between the genotypes. Before comparisons between genotypes could be conducted, it was necessary to derive an approach to compare spectral data that could be applicable to all spectra. Criteria for including and rejecting spectra were developed. Next, it was necessary to determine whether the cortical locations selected for spectral analysis could impact the statistical interpretation of the full data set. After an approach was determined and the effect of spatial locations assessed, statistical analyses were performed to compare spectral indications of degree of bone mineralization and degree of carbonation in the bone mineral of the cKO and the WT mice.

<u>General Comments</u>

173 Raman spectra were collected (130 on humeri; 43 on femora). Carbonated hydroxylapatite (CHAP) was the only mineral detected in the WT and the cKO specimens for both the humeri and the femora. In addition, CHAP was also the only mineral present in the ulna.

The spectra from the humeri and femora had atypically low fluorescence due to the preparation technique. The ulna (prepared by another lab) had significantly higher fluorescence than the humeri and femora. The spectral features in the collagen region for the majority of the spectra

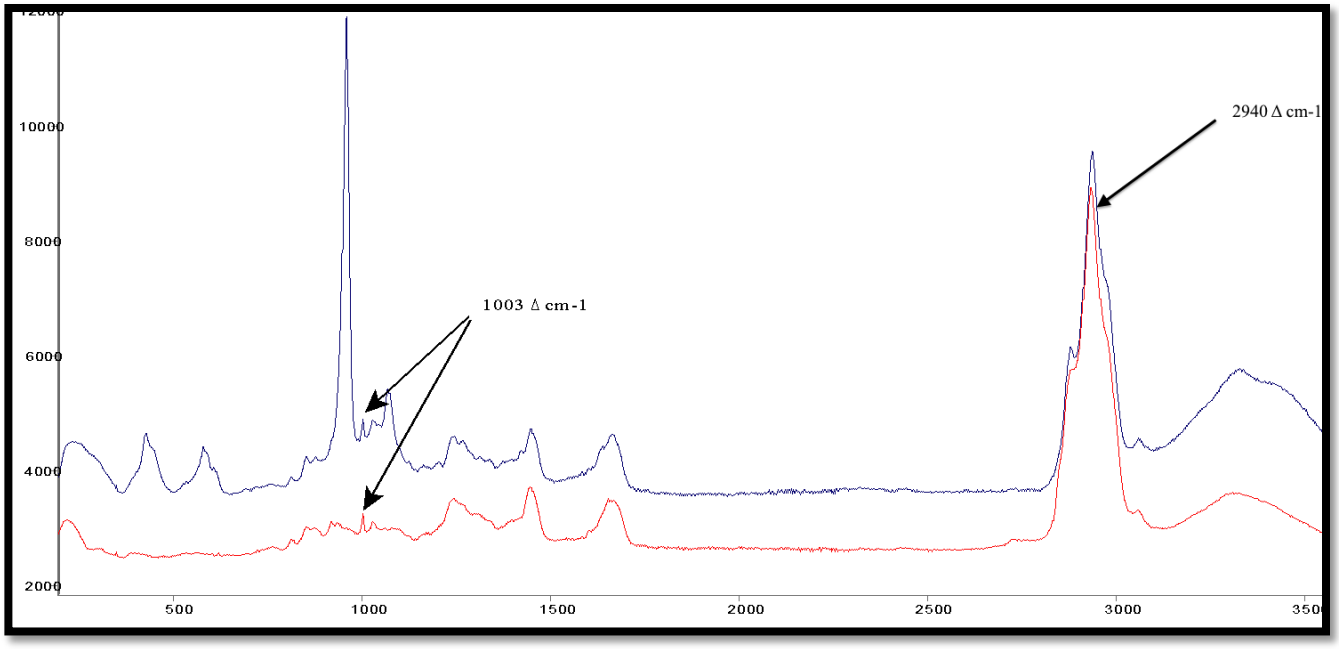

Figure 3.1: Comparison of Raman spectra of pure bovine type I collagen (red) and mouse bone (blue). Arrows indicate peaks at 1003Δcm^{-1} for phenyl group and for 2940 Δcm^{-1} for C-H stretch.

resembled those of pure type I collagen (see Figure 3.1). In several spectra, however, the collagen region differed significantly from the normal. For example, see Figure 3.2 and Figure 2.5. The cause of these abnormalities was not determined, but may represent chemical modifications of the collagen framework or a contamination. These abnormalities were seen in both cKO and WT mice and thus are not a consequence of the genetic modification.

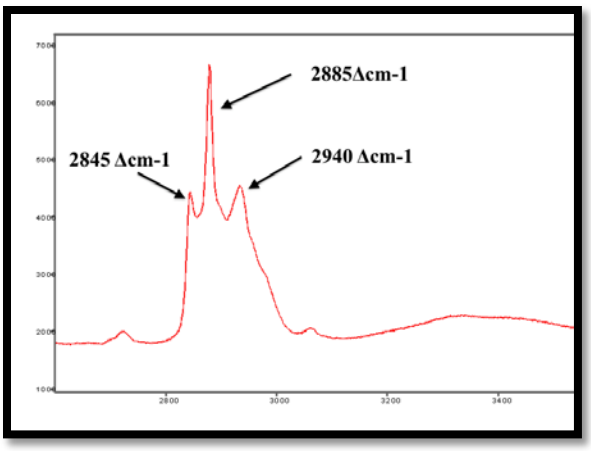

Figure 3.2:
Example of spectrum with abnormal collagen region.

Data Preparation

Three factors were considered in the preparation of the data for analysis: 1) the presence of an additional peak at 2845Δ cm^{-1} in the collagen region (see Figure 3.2); 2) specific cortical region analyzed; and 3) from which side of the body the bone was harvested. The additional peak at 2845 Δcm^{-1} resulted in changes in the measured/derived parameters for other peaks in the collagen region. Multiple analyses were recorded for each mouse, including in different cortical regions and on different sides of the body. After an assessment of individual variability across these sites, these measurements and observations were combined for the final analyses.

1) Peak at 2845 Δcm^{-1}

Almost one quarter of the spectra (28 humeri spectra and 10 femora spectra) collected contained an extra peak in the collagen region, with a median peak position of 2845.4 Δcm^{-1}. The peak position varied from 2843.6 Δcm^{-1} to 2849.6 Δcm^{-1}. The relative intensity of the peak varied significantly within both the humeri and the femora samples (see Figure 3.3).

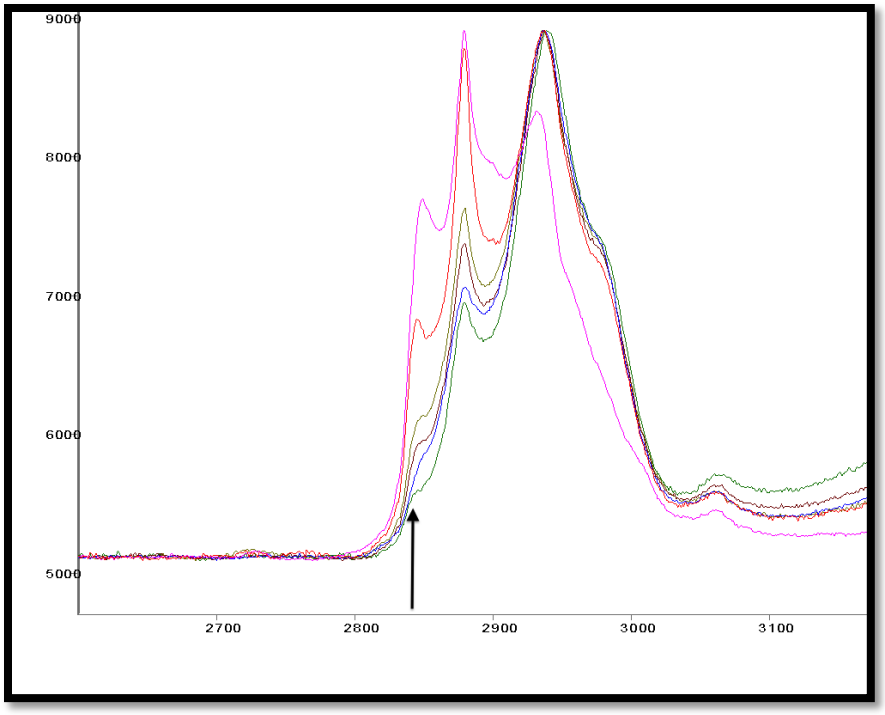

Figure 3.3: Overlay of six spectra, illustrating the variability of the peak at 2845 Δcm^{-1}. Arrow indicates location of this additional peak.

The identity of this peak could not be determined. The spectra with a peak at 2845 Δcm^{-1} came from both WT and cKO mice, indicating that it was not caused by genetic modification. In addition, spectra that had a peak at 2845 Δcm^{-1} came from every cortical region. Therefore, the presence of a contamination is a possible explanation for the presence of this peak with position at 2845 Δcm^{-1}, which varies in intensity. However, since all bones were prepared similarly and all bones that had spectra with this extra peak also had spectra without it, contamination is an unlikely explanation. Another potential explanation is chemical remodeling within the collagen framework, for example, oxidation or reduction of a C-H bond. Typical spectra that do not contain a peak 2845 Δcm^{-1} frequently do have a slight "shoulder" in the vicinity of 2845 Δcm^{-1} (see Figure 3.4). This suggests there is a chemical-molecular reality in some bone that is represented by a spectral feature at 2845 Δcm^{-1} that varies in intensity. The absence of this peak may be explained by the magnitude of the adjacent peak at 2885 Δcm^{-1}, which could engulf the smaller 2845 Δcm^{-1} peak. In this case, the peak at 2845 Δcm^{-1} is only seen in spectra in which it is sufficiently intense. In addition, the peak at 2845 Δcm^{-1} may represent a small microscale

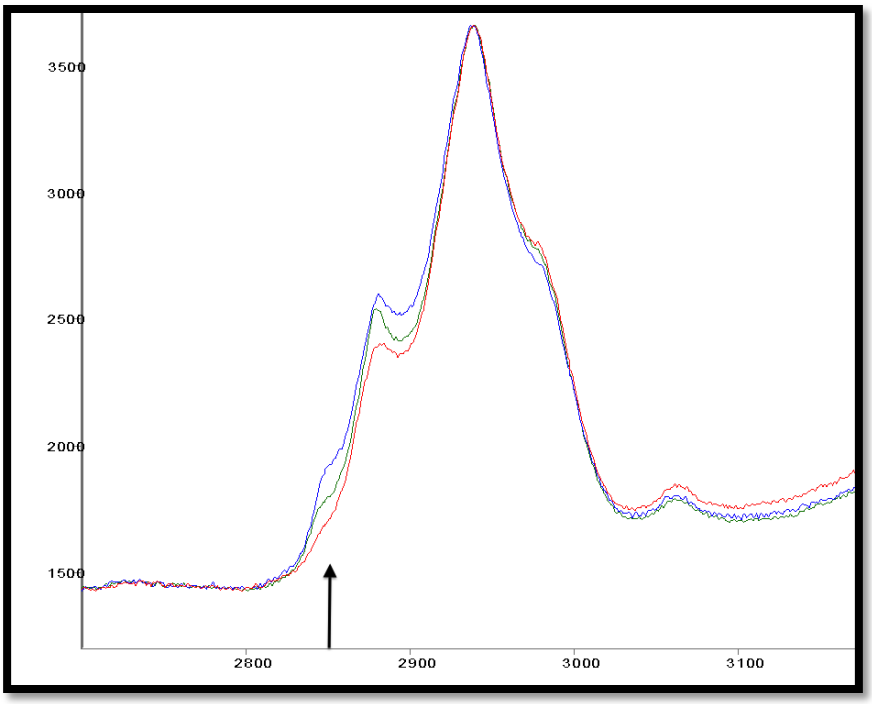

Figure 3.4: Overlay of three spectra. For this study, the spectra in blue and green were deconvolved separately with and without the explicit inclusion of a band at 2845 Δcm^{-1}. The spectrum in red was deconvolved ignoring the extra peak. Expansion of the collagen region demonstrates the presence of a "shoulder," or region of inflection at 2845 Δcm^{-1} indicated by the arrow.

change within the collagen framework that is not present throughout the bone as a whole, or may simply represent a contamination.

The characteristics of another collagen peak were examined in relation to the presence of the 2845 Δcm^{-1} peak to determine whether the latter peak could represent a change within the collagen structure. The peak position and bandwidth of the peak for the phenyl group (1003 Δcm^{-1}) were examined. Its peak position did not vary between the spectra that did and did not have a peak at 2845 Δcm^{-1}. The mean width of the 1003 Δcm^{-1} deconvolved band was larger by 0.60 wavenumbers (10.55 vs. 9.95 wavenumbers) for those spectra lacking a peak at 2845 Δcm^{-1}. This difference in bandwidth suggests the collagen may have higher atomic order when this extra peak is present.

All spectra collected were classified into three types: 1) those that did not have the extra peak and were deconvolved normally; 2) those that had a small peak at 2845Δcm^{-1} and could be deconvolved both with and without a band representing the extra peak; and 3) those that had a significantly intense peak at 2845 Δcm^{-1} and could only be deconvolved with the extra band. To determine whether the 2845 Δcm^{-1} peak significantly affected the parameters for the other peaks within the collagen region, the parameters obtained from the deconvolutions with and without recognizing the peak at 2845 Δcm^{-1} were compared. Boxplots of the differences between parameter values in spectra deconvolved with and without a peak at 2845 Δcm^{-1} were constructed. The differences in the width, area, and peak position of the three peaks to the right of the peak at 2845 Δcm^{-1} were plotted. Since comparisons were made between two different deconvolution approaches to the same spectra, the area could be used without looking at it relative to another area, that is, without examining a ratio of two areas. In general, there were substantial differences between the parameter values from the deconvolutions with and without

the peak at 2845 Δcm^{-1}, indicating that the presence of this extra peak impacts the spectral parameters of the adjacent peaks. The area of the 2940 Δcm^{-1} peak was the only parameter in this spectral region that was used for the main analysis. The difference between the areas of the 2940 Δcm^{-1} peak deconvolved without and with recognizing the additional peak ranged broadly in the humeri, but less so in the femora. However, the median difference between areas for both bone types was considerably less than zero, reflecting a substantial dissimilarity between the deconvolution techniques (see Figure 3.5). Since the peak at 2845 Δcm^{-1} has not been noted previously in the literature, data from the standard deconvolution, i.e., without this peak, were used for this study. Furthermore, most of the specimens did not have this peak. However, the substantial difference between the results obtained from the two deconvolution approaches for the specimens with a peak at 2845 Δcm^{-1} is intriguing and deserves future study to investigate potential collagen remodeling.

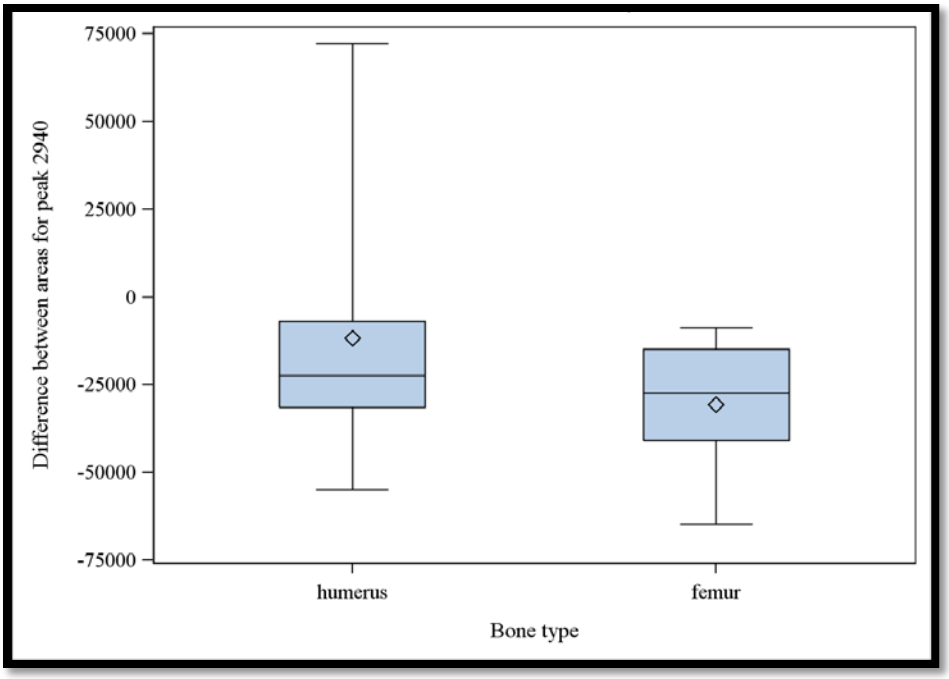

Figure 3.5: Distributions of differences between the calculated areas of the 2940 Δcm^{-1} peak in spectra deconvolved without and with including the peak at 2845 Δcm^{-1}.

The seven spectra that could only be deconvolved by recognizing the peak at 2845Δcm^{-1} were excluded from the final statistical analysis. For the spectra that could be deconvolved with and without the extra peak, only the data from the deconvolutions ignoring 2845Δ cm^{-1} peak were used. The decision to reject data from these seven spectra is supported by the fact that many of the collagen regions already recognized as spectroscopically abnormal also contained a 2845 Δcm^{-1} peak. For example, in Figure 3.3, as the peak at 2845 Δcm^{-1} increases, the adjacent peak increases as well; the spectral region begins to resemble the abnormal collagen in Figure 3.2. Furthermore, Ratio 2 is the only study parameter that utilizes information from the peaks around peak 2845 Δcm^{-1}. Since it uses the area of peak 2940 Δcm^{-1}, conclusions based on Ratio 2 solely should be made with caution.

2) Cortical Region and 3) Body Side

An assessment of whether cortical region or body side impacted the observed molecular-structural characteristics was conducted by comparing the spectral ratios and parameters to be used in the analysis (ratios 1-10; peak position of 960 Δcm^{-1}, and the widths of 960 Δcm^{-1}, 1003 Δcm^{-1}, and 2940 Δcm^{-1}). No spectra that could not be deconvolved without peak 2845 Δcm^{-1} were used for this analysis.

In the humeri, two spectra were collected in three separate cortical regions: inner, middle, and outer as seen in Figure 2.3, resulting in six spectra per humerus. Furthermore, spectra were collected from both the right and left humeri. Therefore, there were twelve spectra collected for each mouse. Boxplots of each combination of cortical area and body side illustrate no substantial differences between cortical regions or body side. While there was a wide range of variability between the different cortical regions and two body sides, there were no trends within the whole sample population that showed differences in spectral features with respect to spatial location in

the bones (see Figures 3.6A and B). In addition, boxplots of all combinations of differences between ratios at different cortical locations within a given mouse were examined to evaluate possible differences between the cortical regions.

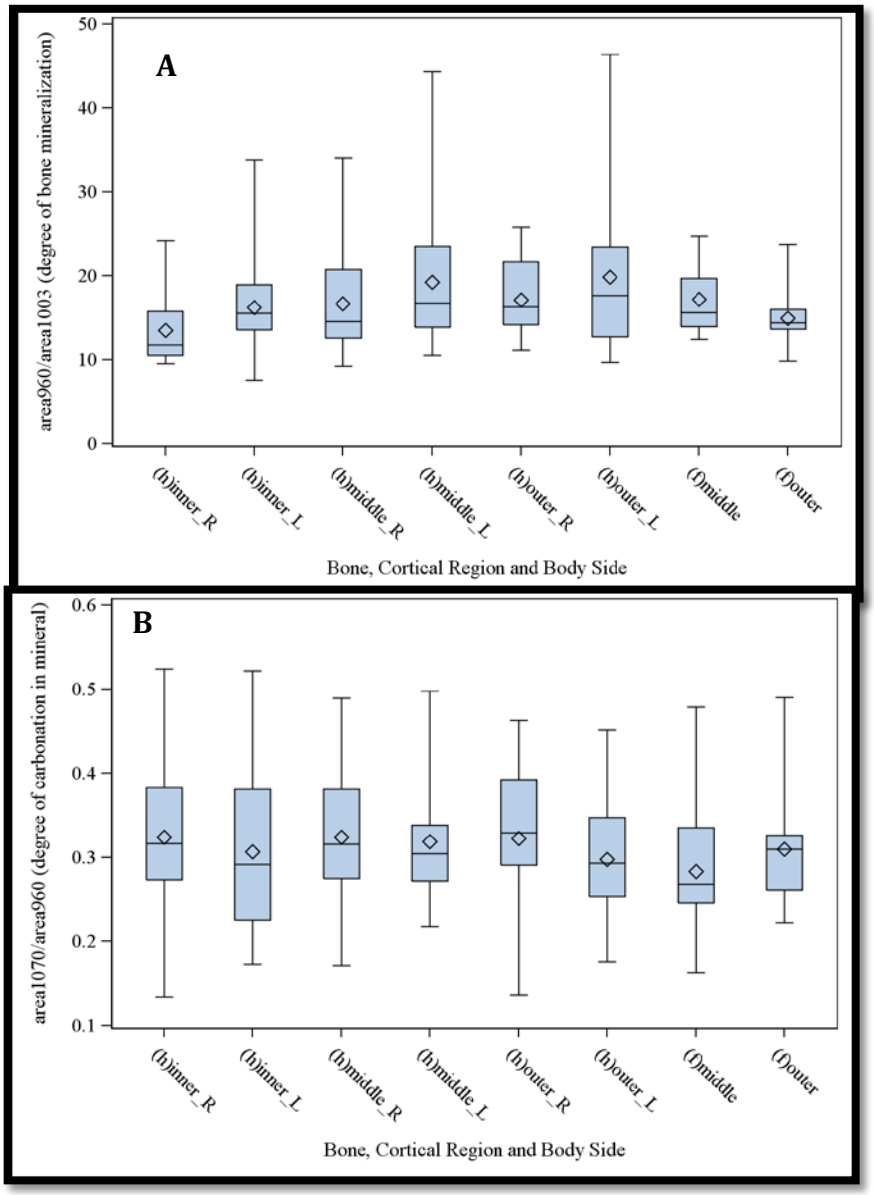

Figures 3.6A and 3.6B: Distributions of Ratios 1 (A) and 6 (B), respectively. For humeri, all combinations of cortical location and body side are displayed. For femora, both cortical locations are shown.

There was considerable variability in the measured parameters. The majority of the means and medians as shown in the boxplots for spectral differences with respect to spatial position of analysis site were centered around zero. These results indicate that there was not a significant difference between the cortical regions for any given mouse (see

Figure 3.7). The inner cortical region unfortunately had higher fluorescence than the other two regions, which degraded the signal-to-noise ratio (i.e., quality) of those spectra.

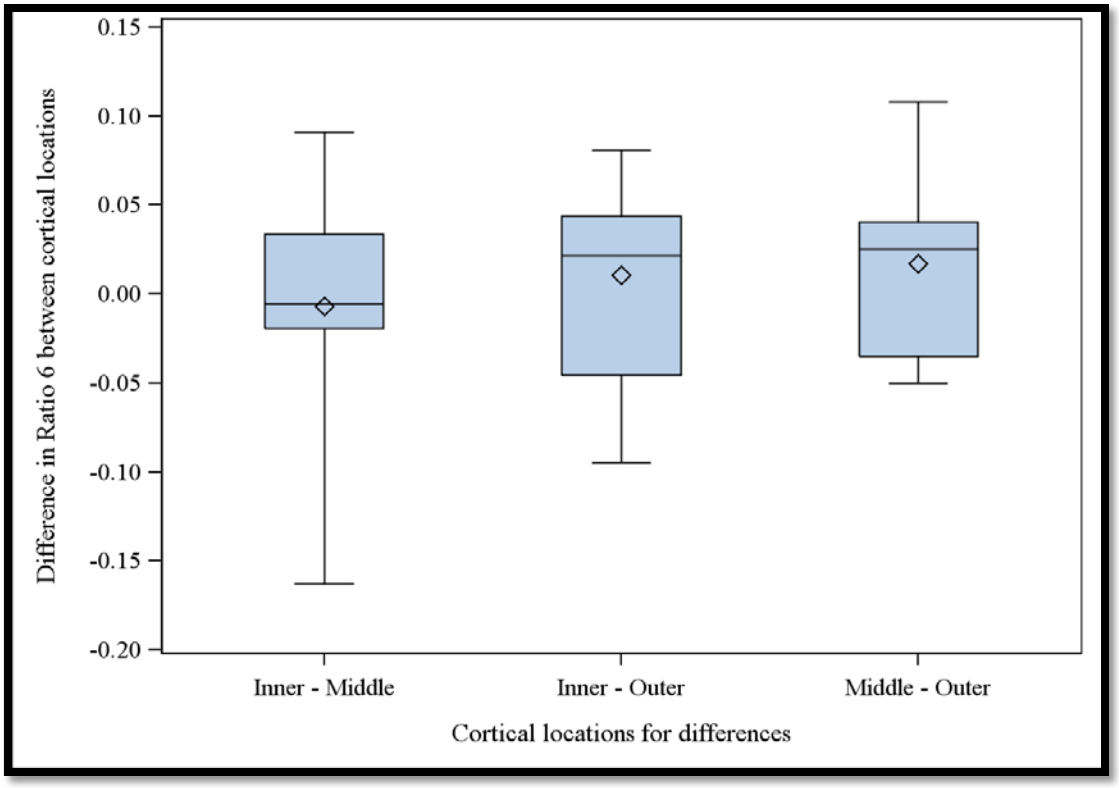

Figure 3.7: Differences in Ratio 6 between cortical locations in humeri.

Due to the high fluorescence in the inner cortical region of the humeri and the similarity in values between the cortical regions and the right- and left-side bones, spectra were collected from only the middle and outer cortical regions of either the right or left femora. There were, therefore, four spectra per mouse for the 12-week-old cohort. Boxplots of the different cortical regions show that there were no substantial differences between the two regions (see Figures 3.6A and B). In addition, the variability in the values of the spectral ratios was similar to that found in the humeri.

Data Preparation: Conclusions

Only data from spectra without a deconvolved peak at 2845 Δcm^{-1} were used in the final statistical analysis. Comparisons between bone regions and between the right and left bones of the same mouse were strictly descriptive, and showed no substantial differences between measurements from these different regions. Several of the spectral parameters showed a few outliers (see Table 3.1), which could significantly affect average values in such a limited data set. Therefore, medians were calculated for all measurements made on a mouse, i.e., the median for each parameter was calculated over all 12 humeri spectra for a given mouse and all 4 femora spectra. Although Akkus et al. (2004) suggested that degree of carbonation may be different between cortical locations, the spectra in this study did not show any consistent or substantial differences between cortical regions. Therefore, the median values for all spectra were calculated and used in all statistical analyses.

Parameter	Humeri		Femora		Ulna	Total
	cKO	WT	cKO	WT		
Number of Spectra	59	65	15	24	4	167
Number of Spectra with Outliers						
Ratio 1	1	2	0	0	0	3
Ratio 2	2	0	0	0	0	2
Ratio 3	0	2	0	0	0	2
Ratio 4	1	0	0	0	0	1
Ratio 5	1	0	0	0	0	1
Ratio 7	1	0	0	0	0	1
Ratio 8	1	0	0	0	0	1
Ratio 10	2	1	0	0	0	3
Total number of outliers	9	5	0	0	0	14

Table 3.1: Summary of outliers. Outliers were defined as observations that deviated more than 3 standard deviations from the mean for all spectra for the cohort/genotype combination.

The results from the Raman analysis of this study will now be presented based on the protocol described above.

Humeri (24-week-old cohort)

A total of 130 spectra were collected for this cohort. Three spectra, each from a separate mouse, were excluded because deconvolutions could not be performed on the collagen region (i.e., the collagen region was abnormal). Three additional spectra were excluded because they could not be deconvolved without a 2845 Δcm^{-1} peak. Therefore, 124 spectra were used in the analysis. There were 10-12 spectra per mouse. Medians were calculated from values of all spectra taken on a mouse.

Carbonated hydroxylapatite was the only mineral present in both the WT and the cKO specimens. The position of the deconvolved 960 Δcm^{-1} band ranged from 960.6 to 961.0 wavenumbers, which is normal for bone. This range indicates some small variability in the chemical components of the bone mineral, for instance by sodium incorporation as a result of carbonate substitution (Skinner, 2005). However, the median band positions were not statistically different between genotypes ($p=0.29$). Similarly, the 960 Δcm^{-1} bandwidth varied only slightly, indicating a small difference in atomic order that was not statistically different ($p=0.99$) by genotype.

Mineral-to-Matrix Ratio

The spectral variables for assessing the mineral-to-matrix (collagen) ratio are summarized in Table 3.2. All measurements indicate that this ratio was higher in the WT than in the cKO. The most reproducible representation is Ratio 1. A comparison between the two genotypes indicates that the mean Ratio 1 for WT (17.0) was greater than that for the cKO (14.1), and the difference was statistically significant ($p=0.04$). Ratios 2, 3, 4, and 5 indicated a similar relation

and, except for Ratio 3, the differences were statistically significant between genotypes, supporting the hypothesis that there is an association between the mineral-to-matrix ratio and genotype among 24-week-old mice. Overall, the WT mice appear to have a higher degree of bone mineralization than the cKO mice, based on analysis of humeri from 24-week-old mice.

Ratio	WT (n=6)		cKO (n=5)		Difference (WT - cKO)		
	mean	95% CI	mean	95% CI	difference	95% CI	p-value
Ratio 1 (area960/area1003)	16.99	14.77, 19.22	14.12	12.03, 16.22	2.87	0.21, 5.52	**0.04**
Ratio 2 (area960/area2940)	0.47	0.43, 0.52	0.39	0.34, 0.44	0.08	0.03, 0.14	**0.01**
Ratio 3 (area950 + area960)/area1003)	28.52	23.15, 33.88	24.88	23.90, 25.86	3.64	-1.63, 8.91	0.15
Ratio 4 (area950 + area960)/area2940)	0.77	0.70, 0.83	0.67	0.58, 0.75	0.10	0.01, 0.19	**0.03**
Ratio 5 (height960/ height1003)	12.72	11.67, 13.77	10.86	10.20, 11.53	1.86	0.73, 2.99	**0.005**

Table 3.2: Ratios of spectral parameters used to assess mineral-to-matrix ratios for 24-week-old cohort (humeri). Bolded values indicate statistical significance ($p \leq 0.05$).

Carbonation

The spectral variables sensitive to carbonate substitution (carbonation) are summarized in Table 3.3. Ratio 6 represents Type B substitution, the primary mechanism of carbonate incorporation in bone mineral. A comparison between the two genotypes indicates that the mean Ratio 6 for the WT (0.31) was less than that for the cKO (0.32), but that the difference was not statistically significant (p=0.64). Ratio 7 also represents Type B substitution, and the difference between genotypes also was not statistically significant (p=0.96). The degree of total carbonation by both substitution mechanisms, Type A and Type B, (Ratio 9) was higher in cKO (0.38) than in the WT (0.35), but the difference was not statistically significant (p=0.31). Ratio 10 also represents the degree of total carbonation, and similarly the difference between genotypes was not statistically significant (p=0.73). A comparison of the proportion of Type B carbonation to

total carbonation (Ratio 8) was not statistically different between genotypes (p=0.30). Type B carbonation represented a substantial proportion of the total carbonation, as would be expected (see Table 3.3). None of these measures of degree or mechanism of carbonation suggest an association between carbonate substitution and genotype.

Ratio	WT (n=6)		cKO (n=5)		Difference (WT - cKO)		
	mean	95% CI	mean	95% CI	Difference	95% CI	p-value
Ratio 6 (area1070/area960)	0.31	0.27, 0.35	0.32	0.26, 0.38	-0.01	-0.07, 0.05	0.64
Ratio 7 (area1070/(area950+ area960))	0.18	0.16, 0.21	0.18	0.17, 0.19	0.00	-0.02, 0.02	0.96
Ratio 8 (area1070/(area1070 +area1100))	0.89	0.87, 0.90	0.87	0.82, 0.91	0.02	-0.02, 0.06	0.30
Ratio 9 ((area1070 + area1100)/area960)	0.35	0.29, 0.40	0.38	0.32, 0.44	-0.03	-0.10, 0.04	0.31
Ratio 10 ((area1070 + area1100)/ (area950 + area960))	0.21	0.19, 0.23	0.22	0.20, 0.23	0.00	-0.03, 0.02	0.73

Table 3.3: Ratios of spectral parameters used to assess the degree of bone mineral carbonation for 24-week-old cohort (humeri).

Femora (12-week-old cohort)

A total of 43 spectra were collected for this cohort. Four spectra were excluded because they could not be deconvolved without a 2845 Δcm^{-1} peak. Therefore, 39 spectra were used in the analysis. There were 2-4 spectra per mouse. Medians were calculated from values of all spectra taken on a mouse.

Carbonated hydroxylapatite was the only mineral present in the WT and the cKO specimens. The position of the deconvolved 960 Δcm^{-1} band ranged from 960.5 to 961.3 wavenumbers, similar to that in the humeri. As with the humeri, the median band positions were not statistically different between genotypes (p=0.92). There was a small difference in atomic

order (the 960 Δcm^{-1} bandwidth) between WT (15.5 wavenumbers) and cKO (15.8 wavenumbers), but this was not a statistically significant difference (p=0.25).

Mineral-to-Matrix Ratio

The spectral variables for assessing the mineral-to-matrix (collagen) ratio are summarized in Table 3.4. There were no apparent differences between the WT and the cKO. For Ratio 1, a comparison between the two genotypes indicates that the mean Ratio 1 for cKO (17.24) was greater than that for the WT (15.61), but the difference was not statistically significant (p=0.37). Ratio 2, which references a different spectral region for collagen, showed the opposite relation, with a higher mean ratio for WT than cKO. However, the difference between genotypes was not statistically significant (p=0.81). Ratio 5 showed a relation similar to that in Ratio 1, as might be expected, since area and height are related, and the difference between genotypes was not statistically significant (p=0.55). For the various measures of the mineral-to-matrix ratio there were no statistically significant differences between the genotypes. Spectroscopically, there is not a definable association between the mineral-to-matrix ratio and the genotype among femora from 12-week-old mice, in contrast to the results for the humeri from 24-week-old mice.

Ratio	WT (n=7)		cKO (n=4)		Difference (WT - cKO)		
	mean	95% CI	mean	95% CI	difference	95% CI	p-value
Ratio 1 (area960/area1003)	15.61	14.05, 17.18	17.24	10.74, 23.74	-1.63	-5.50, 2.25	0.37
Ratio 2 (area960/area2940)	0.46	0.40, 0.52	0.45	0.42, 0.49	0.01	-0.07, 0.08	0.81
Ratio 3 (area950 + area960)/area1003)	26.17	23.69, 28.66	30.35	13.88, 46.81	-4.17	-13.20, 4.85	0.32
Ratio 4 (area950 + area960)/area2940)	0.78	0.72, 0.84	0.78	0.64, 0.92	0.00	-13.20, 4.85	0.93
Ratio 5(height960/ height1003)	12.65	11.87, 13.43	12.99	11.44, 14.55	-0.35	-1.61, 0.91	0.55

Table 3.4: Ratios of spectral parameters used to assess mineral-to-matrix ratios for 12-week-old-cohort (femora).

Carbonation

The spectral variables sensitive to carbonation in bone mineral are summarized in Table 3.5. There were no apparent differences between genotypes for Type B substitution. For Ratio 6, the mean for the WT (0.31) was higher than that for the cKO (0.30). The reverse relation was seen for Ratio 7, for which the mean was higher for cKO (0.18) than WT (0.17). Neither difference, however, was statistically significant (p=0.84 and p=0.42, respectively). The two ratios representing the degree of total carbonation (Ratios 9 and 10) did not show differences between genotypes that were statistically significant (Table 3.5). The proportion of Type B carbonation in the total carbonation (Ratio 8) was not statistically different between genotypes (p=0.13). Type B carbonation represented a substantial proportion of the total carbonation, as would be expected (see Table 3.5). None of these spectral measures of carbonation suggests an association between carbonate substitution and genotype for femora from 12-week-old mice.

Ratio	WT (n=7)		cKO (n=4)		Difference (WT - cKO)		
	mean	95% CI	mean	95% CI	difference	95% CI	p-value
Ratio 6 (area1070/area960)	0.31	0.23, 0.38	0.30	0.25, 0.35	0.01	-0.09, 0.11	0.84
Ratio 7 (area1070/ (area950+area960))	0.17	0.15, 0.19	0.18	0.16, 0.20	-0.01	-0.04, 0.02	0.42
Ratio 8 (area1070/ (area1070+area1100))	0.88	0.84, 0.91	0.91	0.89, 0.93	-0.03	-0.07, 0.01	0.13
Ratio 9 ((area1070 + area1100)/area960)	0.35	0.28, 0.42	0.33	0.28, 0.37	0.02	-0.07, 0.12	0.56
Ratio 10 ((area1070 + area1100)/ (area950 + area960))	0.19	0.18, 0.21	0.20	0.17, 0.22	0.00	-0.03, 0.02	0.79

Table 3.5: Ratios of spectral parameters used to assess the degree of bone mineral carbonation for 12-week-old cohort (femora).

Comparison between age-cohorts

The 24-week-old cohort was compared to the 12-week-old cohort to examine the effect of age on molecular-structural characteristics. Different bones (humeri and femora) were utilized

for these cohorts. Therefore, this comparison is based on the assumption that differences between cohorts are not due to the type of bone, but rather the age of the mouse. While material characteristics vary substantially between different types of bones, the femur and humerus are large, weight-bearing bones in mice. Their similar purpose should result in comparable material characteristics. However, this assumption should be recognized when interpreting the results. Furthermore, since mice were sacrificed, they could not be monitored over time. Therefore, comparisons presented here do not examine trends over an individual's lifetime, but rather the trends at a population level.

All ten ratios showed no statistically significant differences between the 12-week-old WT and 24-week-old WT (Tables 3.6 and 3.7). However, for the cKO, a couple of ratios were statistically different between the two age cohorts, and several were borderline in significance (Tables 3.8 and 3.9). Two ratios (Ratios 2 and 5) demonstrating statistically significant differences with age suggest there is a decrease in the mineral-to-matrix ratio with age in the cKO. The other ratios, including Ratio 1, showed a relation with age similar to that for Ratio 5, with a lower mineral-to-matrix ratio in the 24-week-old cohort. In fact, the difference between the age cohorts in the cKO for Ratio 1 was larger than that for the difference between the genotypes in the humeri (2.87), which itself was statistically significant (Table 3.2). These results suggest a decrease in the mineral-to-matrix ratio with age in the cKO. In normal bone, the reverse trend is seen; the degree of mineralization increases with age (Legros et al., 1987; Akkus et al., 2004; Glimcher, 2006). Since there was no mineralization difference by age in WT bone, the differences seen between the two ages of cKO cohorts may be due to genotype-dependent processes. For example, there may be differences in maturation processes or rates between the two genotypes.

Ratio	24-week-old (n=6)		12-week-old (n=7)		24-week-old - 12-week-old		
	mean	95% CI	mean	95% CI	difference	95% CI	p-value
Ratio 1 (area960/area1003)	16.99	14.77, 19.22	15.61	14.05, 17.18	1.38	-0.95, 3.70	0.22
Ratio 2 (area960/area2940)	0.47	0.43, 0.52	0.46	0.40, 0.52	0.01	-0.06, 0.08	0.78
Ratio 3 (area950 + area960)/area1003)	28.52	23.15, 33.88	26.17	23.69, 28.66	2.34	-2.53, 7.21	0.31
Ratio 4 (area950 + area960)/area2940)	0.77	0.70, 0.83	0.78	0.72, 0.84	-0.02	-0.10, 0.06	0.67
Ratio 5 (height960/ height1003)	12.72	11.67, 13.77	12.65	11.87, 13.43	0.08	-1.05, 1.20	0.88

Table 3.6: Ratios of spectral parameters used to assess mineral-to-matrix ratios for WT. Humeri of the 24-week-old cohort and femora of the 12-week-old cohort were analyzed.

Ratio	24-week-old (n=6)		12-week-old (n=7)		24-week-old - 12-week-old		
	mean	95% CI	mean	95% CI	difference	95% CI	p-value
Ratio 6 (area1070/area960)	0.31	0.27, 0.35	0.31	0.23, 0.38	0.00	-0.08, 0.08	0.98
Ratio 7 (area1070/ (area950+area960))	0.18	0.16, 0.21	0.17	0.15, 0.19	0.01	-0.01, 0.04	0.25
Ratio 8 (area1070/ (area1070+area1100))	0.89	0.87, 0.90	0.88	0.84, 0.91	0.01	-0.03, 0.05	0.57
Ratio 9 ((area1070 + area1100)/area960)	0.35	0.29, 0.40	0.35	0.28, 0.42	0.00	-0.09, 0.08	0.92
Ratio 10 ((area1070 + area1100)/ (area950 + area960))	0.21	0.19, 0.23	0.19	0.18, 0.21	0.02	0.00, 0.04	0.10

Table 3.7: Ratios of spectral parameters used to assess the degree of bone mineral carbonation for WT. Humeri of the 24-week-old cohort and femora of the 12-week-old cohort were analyzed.

Ratio	24-week-old (n=6)		12-week-old (n=7)		24-week-old - 12-week-old		
	mean	95% CI	mean	95% CI	difference	95% CI	p-value
Ratio 1 (area960/area1003)	14.12	12.03, 16.22	17.24	10.74, 23.74	-3.12	-7.82, 1.58	0.16
Ratio 2 (area960/area2940)	0.39	0.34, 0.44	0.45	0.42, 0.49	-0.07	-0.12,-0.02	0.02
Ratio 3 (area950 + area960)/area1003)	24.88	23.90, 25.86	30.35	13.88, 46.81	-5.47	-16.26, 5.32	0.27
Ratio 4 (area950 + area960)/area2940)	0.67	0.58, 0.75	0.78	0.64, 0.92	-0.11	-0.23, 0.01	0.06
Ratio 5 (height960/ height1003)	10.86	10.20, 11.53	12.99	11.44, 14.55	-2.13	-3.33, -0.93	0.004

Table 3.8: Ratios of spectral parameters used to assess mineral-to-matrix ratios for cKO. Humeri of the 24-week-old cohort and femora of the 12-week-old cohort were analyzed.

Ratio	24-week-old (n=6)		12-week-old (n=7)		24-week-old - 12-week-old		
	mean	95% CI	mean	95% CI	difference	95% CI	p-value
Ratio 6 (area1070/area960)	0.32	0.26, 0.38	0.30	0.25, 0.35	0.02	-0.04, 0.09	0.45
Ratio 7 (area1070/(area950+area960))	0.18	0.17, 0.19	0.18	0.16, 0.20	0.00	-0.01, 0.02	0.64
Ratio 8 (area1070/ (area1070+area1100))	0.87	0.82, 0.91	0.91	0.89, 0.93	-0.04	-0.09, 0.00	0.07
Ratio 9 ((area1070 + area1100)/area960)	0.38	0.32, 0.44	0.33	0.28, 0.37	0.05	-0.01, 0.12	0.09
Ratio 10 ((area1070 + area1100)/ (area950 + area960))	0.22	0.20, 0.23	0.20	0.17, 0.22	0.02	0.00, 0.04	0.08

Table 3.9: Ratios of spectral parameters used to assess the degree of bone mineral carbonation for cKO. Humeri of the 24-week-old cohort and femora of the 12-week-old cohort were analyzed.

The effect of carbonate substitution on atomic order

Carbonate can substitute for phosphate and or hydroxyl in the CHAP lattice. Both of these substitutions cause distortion of the crystalline framework (Ivanova et al., 2000). Distorting the framework results in a reduction of crystallinity as seen in increasing atomic order, which is represented by the bandwidth of the 960 Δcm^{-1} peak. The more ordered a material, the smaller its bandwidth. In synthetic CHAP, there is a strong positive correlation between degree of carbonation and bandwidth of the 960 Δcm^{-1} peak (deMul et al., 1988), as would be expected for decreasing crystallinity. In biological CHAP, however, both carbonation and crystallinity increase concurrently with age (Akkus et al., 2004). The differences between synthetic and biologic CHAP undoubtedly result in part from the continual remodeling of bone during an organism's lifetime.

There was a strong negative correlation between the degree of carbonation and the bandwidth of the 960 Δcm^{-1} peak for the cKO and WT mice (Figure 3.8; all acceptable spectra for each mouse were included). This inverse relationship was summarized by the Spearman

correlation for each the four bone groups and two genotypes, which ranged from -0.75 to -0.59. While the cohorts showed the trend expected for CHAP during maturation of bone, the mice within each cohort were almost exactly the same age. Within an age cohort, there will be some variability in the biological level of maturity. Therefore, this trend may reflect differences in maturation stage rather than just age. However, there is a strong association between age and maturity, and one would expect that the mice from the 24-week-old cohort would have more mature bones than those from the 12-week-old cohort. There was no readily recognizable difference between the age-cohorts in this relation. This is not surprising, as there were no significant differences between the age cohorts for degree of carbonation or crystallinity. I am unaware that this trend has been shown for a cohort of animals of the same age. Therefore, this relation (Figure 3.8) should be an area of further inquiry.

There are a few possible explanations for this trend other than maturity of an organism. Tissue age varies spatially within bones. For example, new bone material is laid down on the surface of the existing bone, and thus one would expect to find younger, less mature tissue in these locations than in the middle of the cortex. While the observed trend (Figure 3.8) could reflect these spatial differences, similar trends were seen for each cortical location. Therefore, this study does not support the explanation that the observed trend is due to differences in tissue age, at least at the level examined in this study.

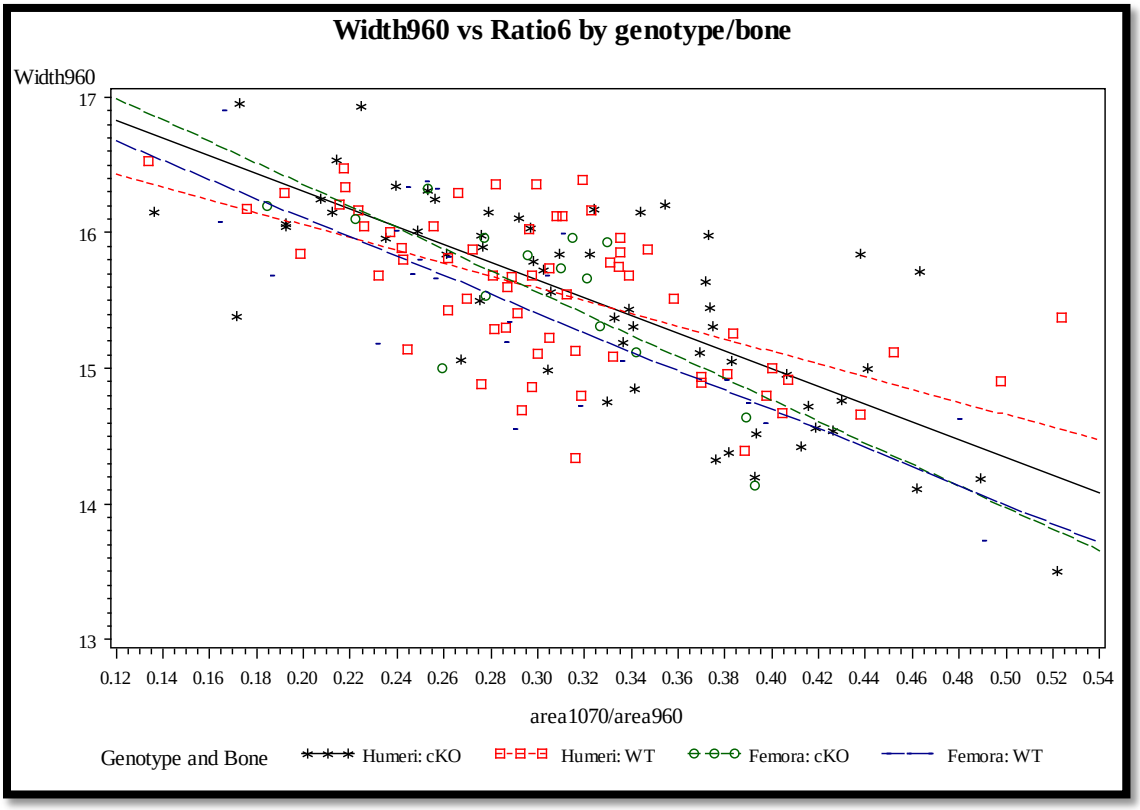

Figure 3.8: Degree of atomic order and crystallinity (as represented by width960) vs. carbonation (Ratio 6) for each genotype and bone combination.

Comparison with the ulna

Carbonated hydroxylapatite was the only mineral present in the spectra obtained from the ulna specimen. The position of the deconvolved 960 Δcm^{-1} band ranged from 960.6 to 961.4 wavenumbers, similar to that observed with the medians for the humeri and femora. Furthermore, there was a small range in atomic order (the 960 Δcm^{-1} bandwidth) between spectra. The median 960 Δcm^{-1} bandwidth was substantially smaller in the ulna (12.61 wavenumbers) than in the femora (15.65 wavenumbers) and humeri (15.66 wavenumbers). A smaller 960 Δcm^{-1} bandwidth suggests greater crystallinity in this ulna compared to the other bones.

Since data was collected from only one ulna, no statistical tests were performed for the comparison between it and the bones from this study. Instead, strictly descriptive comparisons were made between the different types of bone and genotype. All spectra that had not been

excluded in the data preparation were included, rather than restricting the comparisons to the medians for each mouse. Therefore, the four ulna spectra were compared with the 124 humeri spectra and 39 femora spectra. Most ratios for the ulna fell below the 25th percentile for the other bones (e.g., Figure 3.9), suggesting that there were considerable material and mineral differences between the ulna and the cKO and WT bones of this study. However, the ranges of Ratios 6, 9, and 10 were similar between those of the other bones and the ulna (see Figure 3.10), suggesting that the degree of carbonation, particularly of Type B, was similar between the bones.

Unlike Type B carbonation, there appeared to be a considerable difference in Type A carbonate substitution between the bones. The proportion of Type A carbonate substitution was represented by the ratio of Type A carbonation to overall carbonation: Area1100/(Area1100+Area1070). The range of the proportion of Type A carbonation in the ulna lay within that for the other bones, but the proportion of Type A carbonation was, on average, considerably higher in the ulna than in the other bones (see Figure 3.11, Table 3.10). Furthermore, Ratio 8 was also lower in the ulna than in the other bones, as would be expected for a higher Type A carbonate concentration. Although the proportion of Type A carbonation was high in the ulna, Type B carbonation still comprised the majority (74.3%) of the total carbonation, as expected for CHAP (Elliott, 1994; Daculsi et al., 1997). There appeared to be both material and compositional differences between the cKO and WT bones and the ulna. However, due to the small sample size (only four spectra from one ulna were collected), all conclusions should be viewed with caution.

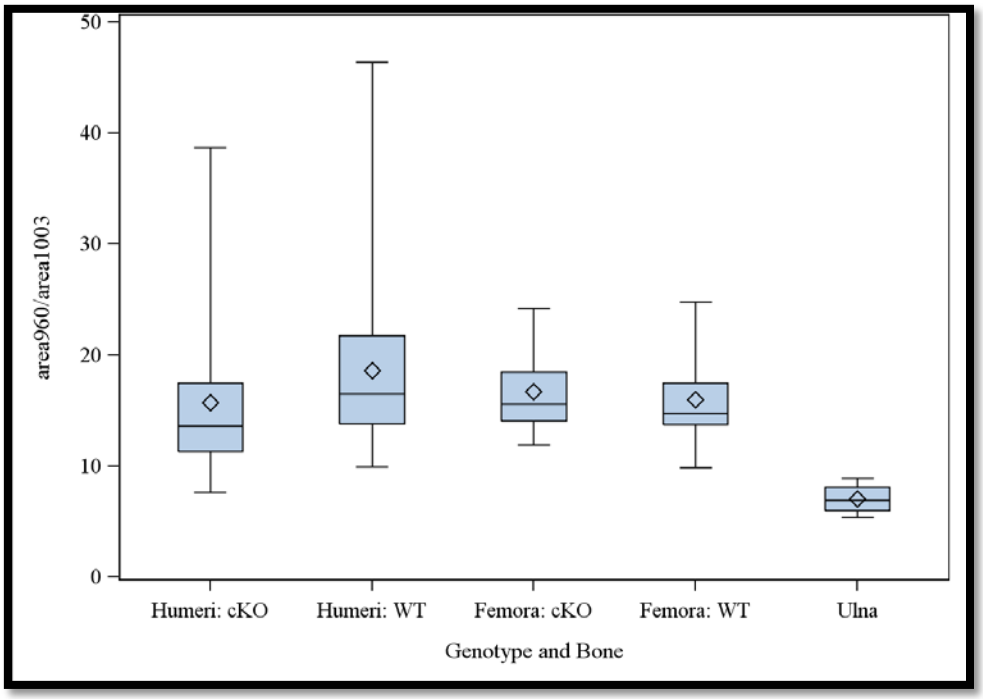

Figure 3.9: Comparison between bones and genotypes for Ratio 1, assessing degree of bone mineralization.

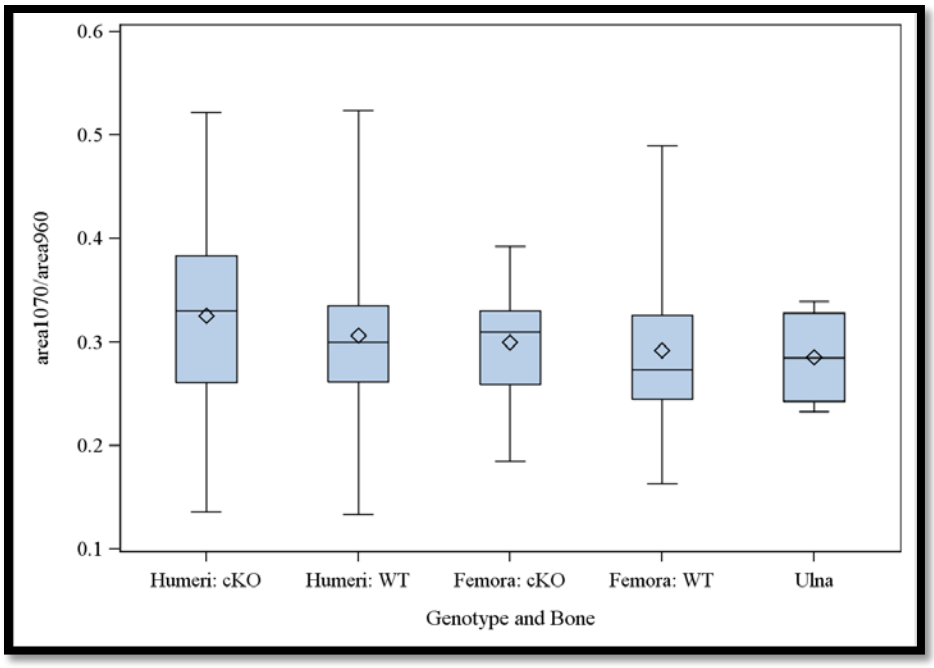

Figure 3.10: Comparison between bones and genotypes for Ratio 6, degree of carbonation in mineral.

Figure 3.11 and Table 3.10: Comparison between bones and genotypes for proportion of Type A carbonate substitution in total substitution

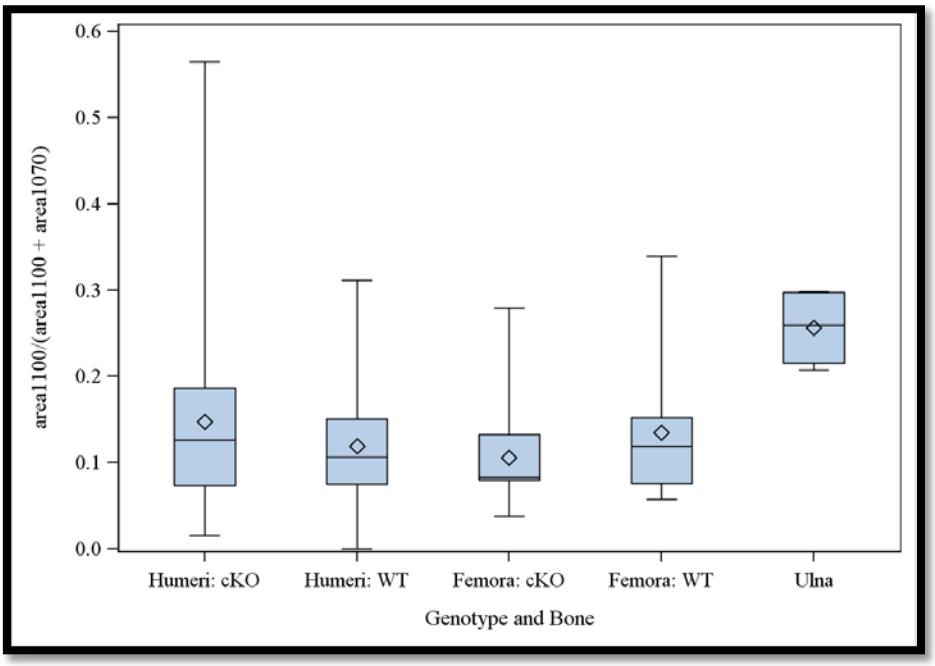

Bone and genotype	Proportion Type A Carbonation		
	Median	Minimum	Maximum
Humeri cKO	0.13	0.02	0.56
Humeri WT	0.11	0.00	0.31
Femora cKO	0.08	0.04	0.28
Femora WT	0.12	0.06	0.34
Ulna	0.26	0.21	0.30

Chapter 4 - Concluding Remarks

BMP2 expression in osteoblasts is important to post-natal bone growth and strength. BMP2 has a significant impact on the mechanical properties of the bones. While the mineral-to-matrix parameters differed between the genotypes in the 24-week-old mice, these differences were not seen in the femora. There were no differences in carbonation between genotypes for either age. In addition, the conditional knockout did not substantially affect the mineral characteristics of the bone across age. Furthermore, material and compositional characteristics did not differ significantly between age cohorts. The cKO and WT bones from both age cohorts were more similar to each other than to the unrelated ulna, which differed considerably in its mineral-to-matrix ratio, crystallinity, and degree of Type A carbonation.

During maturation in normal bone (documented in human, bovine, and rat bones) there is a well-recognized increase in degree of mineralization, crystallinity, and Type B carbonation (Akkus et al., 2004; Glimcher, 2006). The mice in the two age cohorts in this study did not demonstrate these trends. Instead, there was a reduction in mineral crystallinity with age, albeit the difference was not statistically significant. There was an association between genotype and mineral-to-matrix ratio in 24-week-old mice, but not in 12-week-old mice. Furthermore, the degree of mineralization decreased with age in cKO, suggesting that material maturation processes may be altered in bones lacking BMP2. This conclusion is based on the assumption that the differences between cohorts were due to age, not to the difference in bone type. In addition, the degree of carbonation did not differ between age cohorts in the expected manner; carbonation did not increase from the 12-week-old cohort to the 24-week-old cohort. Furthermore, colleagues observed physical differences in bones and teeth between the age cohorts. Malocclusions in the cKO worsened with age, and the differences in bone characteristics

(e.g., volume and mineral content) that were seen at 12 weeks were absent by 24 weeks. These results indicate that BMP2 plays a role in biomineralization over the course of an organism's life.

A strong association between degree of carbonation and crystallinity was seen in both age cohorts and both genotypes. This trend supports results from other studies that with increasing carbonation there is also an increase in crystallinity. However, this is the first study to show this trend in cohorts of the same age. More research on the relationship between this correlation and maturity should be conducted.

A bone from another lab was used as a comparison for the cKO and WT mouse bones. Overall, this ulna was considerably different from the bones that were the focus of this study. The cKO and WT bones from this study showed both higher mineral-to-matrix ratios and degree of carbonation than did the ulna and showed lower crystallinity than the ulna. In addition, the ulna had a considerably higher proportion of Type A carbonate than did the bones of this study. The level of Type A carbonate substitution in the study mice was within the normal range indicated in the literature (approximately 11% of total), whereas in the ulna, Type A carbonate made up 26% of the total carbonation—more than twice the normal value. However, only one ulna was measured, and thus results about either the ulna or the differences between the ulna and the bones from this study should be interpreted cautiously.

Overall, there were unexpectedly few statistically significant spectral differences between the genotypes. These findings suggest that the mechanical differences measured by my colleagues are not a consequence of modifications in the mineral-to-matrix ratio and the state of the carbonation in the mineral, at least on the scale that can be examined through the Raman spectroscopic techniques employed here and with the number of mice in my study.

Limitations

This study was limited in several ways. There was a relatively small sample size for each age cohort, and there was only one ulna used for comparisons. Comparisons of boxplots indicated no significant differences between different cortical regions of the bones. Therefore, the data analyzed here was compiled over all cortical regions. However, studies have shown there to be differences in degree of carbonation and mineralization in different cortical regions that experience a higher level of stress (Currey, 1996; Akkus et al., 2004).

The mineral-to-matrix ratio has some limitations in representing the material characteristics of bone. This parameter describes the relative proportion of CHAP to collagen, but there are many other factors that affect the material characteristics of bone that are not captured by this parameter. Microscale characteristics of collagen, such as crosslinking, have a profound effect on the chemical and mechanical characterizes of bone as a whole, as well as its formation. In addition, how the mineral and collagen bind, and the strength of these bonds impact the mechanical and chemical characteristics of the structure. Furthermore, the existence of a peak at 2845 Δcm^{-1} for approximately a quarter of the specimens, while intriguing, also resulted in two deconvolutions for the collagen region. The analysis presented here used only one of these, but the alternative deconvolution may prove to be valuable.

More sophisticated statistical models could have been used to account for the multiple measurements for each mouse. However, to properly handle the dependencies created by measurements taken at varying cortical location and side of body would have required mixed ANOVA models, which were outside the scope of my statistical training. Thus, the multiple measurements were summarized using the medians across all spectra for a mouse (other studies

have also used summary statistics) and these summary values were used in the statistical analyses.

Future Directions

The presence of the peak at 2845 Δcm^{-1} has not been previously noted. This peak may represent a chemical contamination that affected the cKO and WT and thus was not found in other mice. Since the collagen region of several spectra that contained this peak was considerably different from normal collagen, this peak may represent a chemical-structural change within collagen that is not present throughout the bone as a whole and that varies with intensity. More studies should be conducted to determine the identity and cause of this spectral phenomenon, especially if it represents a chemical-molecular reality of all collagen that has been overlooked due to the dominance of the adjacent 2885 Δcm^{-1} peak.

Several methodological changes could improve the results from this study. While Raman spectroscopy is an excellent technique for the examination of structural-molecular characteristics of a material, infrared spectroscopy provides better spectra for collagen (Walton et al., 1970). Several ratios were used in this study, but the area of the 1003 Δcm^{-1} was assumed to be the most accurate indicator of the collagen proportion. Many other peaks that represent collagen could have been used in place of or in addition to the 1003 Δcm^{-1} peak. These peaks could have provided other information about the chemical and material characteristics of the cKO and WT bones.

The peaks within the amide region are frequently used to characterize collagen (Paschalis et al., 2001; Paschalis et al., 2006; Nalla et al., 2006; Ager et al., 2006; Buckley et al., 2012; Inzana et al., 2012). In addition, Karampas et al. (2012) developed several calibration models for analyzing the mineral-to-matrix ratio using Raman spectroscopy. They found that proline (855

Δcm^{-1}) and hydroxyproline (875 Δcm^{-1}) were the most accurate indicators for collagen and that the height ratio of 960 Δcm^{-1} to the sum of the bands for proline and hydroxyproline was the most accurate model for the mineral-to-matrix ratio. Proline and amide I and III band profiles are sensitive to post-translational modifications such as crosslinking, and have been used to express such (Buckley et al., 2012; Nalla et al., 2006). The amide, proline, and hydroxylproline peaks were not used in this study because of poor signal. However, these parameters may prove useful in future studies and with different techniques. For example, Ager et al., (2006) used UV excitation coupled with Raman spectroscopy to enhance the intensity of the amide I vibration.

Cross-linking between collagen molecules significantly impacts the structure of collagen. Paschalis et al. (2001) found that the ratio of nonreducible (pyridinium) to reducible cross-links was a better predictor of bone fragility than bone mass density. Cross-linking density also impacts the brittleness of bone (Buehler, 2007). The cross-linking density and ratio of pyridinium to reducible cross-links could explain the mechanical differences seen between the cKO and WT, which could not be captured by the methods employed here. Exploring these factors could be an enlightening next step in determining possible explanations for the mechanical differences seen in this study.

Acknowledgements

I would like to thank Professor Jill Pasteris for her oversight and detailed input and guidance throughout this whole project. I would especially like to thank her for patiently helping me to further understand the principles of mineralogy and Raman spectroscopy. I would like to thank Drs. Matthew Silva and Sara McBride for allowing me to be part of their study, their guidance and feedback on the finished thesis, and for the bone samples that made this study

possible. I also thank Professor Chris Stidley of the University of New Mexico for her help in designing a statistical analysis plan for this study, furthering my understanding of statistics, and her input on statistical interpretations.

Citations

Ager, J.W., Nalla, R.K., Balooch, G., Kim, G., Pugach, M., Habelitz, S., Marshall, G.W., Kinney, J.H., and Ritchie, R.O., (2006). On increasing fragility of human Teeth with age: a deep-UV resonance Raman study. *Journal of Bone and Mineral Research*, 21(12), 1879-1887.

Ager, J.W., Nalla, R.K., Breeden, K.L., and Ritchie, R.O. (2005). Deep-ultraviolet Raman spectroscopy study of the effect of aging on human cortical bone. *Journal of biomedical optics*, 10(3), 034012.

Akkus, O., Adar, F., and Schaffler, M.B., (2004). Age-related changes in physicochemical properties of mineral crystals are related to impaired mechanical function of cortical bone. *Bone*, 34, 443-453.

Alexander, B., Daulton, T.L., Genin, G.M., Lipner, J., Pasteris, J.D., Wopenka, B., and Thomopoulos, S. (2012). The nanometre-scale physiology of bone: steric modelling and scanning transmission electron microscopy of collagen-mineral structure. *Journal of the Royal Society, Interface / the Royal Society*, 9(73), 1774–86.

Baig, A.A., Fox, J.L., Young, R.A., Wang, Z., Hsu, J., Higuchi, W.I., Chhettry, A., Zhuang, H., and Otsuka, M. (1999). Relationships among carbonated apatite solubility, crystallite size, and microstrain parameters. *Calcified tissue international*, 64(5), 437–49.

Biltz, R.M., and Pellegrino, E.D., (1969). The chemical anatomy of bone. *The Journal of Bone and Joint Surgery*, 51A(3), 456-466.

Boskey, A. L. (2007). Mineralization of bones and teeth, *Elements*, (3), 385–392.

Buehler, M.J., (2007). Nanomechanics of collagen fibrils under varying cross-link densities: Atomistic and continuum studies. *Journal of the Mechanical Behavior of Biomedical Materials I*, 59-67.

Buckley, K., Matousek, P., Parker, A.W., and Goodship, A.E. (2012). Raman spectroscopy reveals differences in collagen secondary structure which relate to the levels of mineralisation in bones that have evolved for different functions. *Journal of Raman Spectroscopy*, 43(9), 1237-1243.

Chappuis, V., Gamer, L., Cox, K., Lowery, J.W., Bosshardt, D.D., and Rosen, V. (2012). Periosteal BMP2 activity drives bone graft healing. *Bone*, 51(4), 800–9.

Chen, D., Zhao, M., and Mundy, G.R. (2004). Bone morphogenetic proteins. *Growth factors*, 22(4), 233–41.

Cheng, H., Jiang, W., Phillips, F.M., Haydon, R.C., Peng, Y., Zhou, L., Luu, H.H., An, N., Breyer, B., Vanichakarn, P., Szatkowski, J.P., Park, J.Y., and He, T-C, (2003) Osteogenic activity of the fourteen types of human bone morphogenetic proteins (BMPs). *The Journal of Bone and Joint Surgery*, 85A(8), 1544-1550.

Cormack, D.H., (1998). Clinically Integrated Histology, p. 81-97. Lippencott-Raven, Philadelphia.

Currey, J.D., Brear, K., and Zioupos, P., (1996). The effects of ageing and changes in mineral content in degrading the toughness of human femora. *Journal of Biomechanics*, 29(2), 257-260.

Daculsi, G., Bouler, J-M. and LeGeros, R.Z., (1997). Adaptive crystal formation in normal and pathological calcifications in syntheticic calcium phosphate and related biominerals. *International Review of Cytology*, 172, 129-191.

Deer, W.A., Howie, R.A., Zussman, J., (1996). An Introduction to the Rock-Forming Minerals, p. 506. Longman, London.

deMul, F.F.M, Otto, C., Greve, J., (1988). Calculation of the Raman Line Broadening on Carbonation in Syntetic Hydroxylapatite. *Journal of Raman Spectroscopy*, 19, 13-21.

Devlin, M.J., Cloutier, A.M., Thomas, N.A., Panus, D.A., Lotinun, S., Pinz, I., Baron, R., Rosen, C.J., and Bouxsein, M.L. (2010). Caloric restriction leads to high marrow adiposity and low bone mass in growing mice. *Journal of bone and mineral research : the official journal of the American Society for Bone and Mineral Research*, 25 (9), 2078–88.

Dong, R., Yan, X., Pang, X., and Liu, S. (2004). Temperature-dependent Raman spectra of collagen and DNA. *Spectrochimica Acta Part A: Molecular and Biomolecular Spectroscopy*, 60(3), 557–561.

Einhorn, T.A., Majeska, R.J., Mohaideen, A., Kagel, E.M., Bouxsein, M.L., Turek, T.J. and Wozney, J.M (2003). A single percutaneous injection of recombinant human bone morphogenic protein-2 accelerates fracture repair. *The Journal of Bone and Joint Surgery*, 85A(8), 1425-1434.

Elliott, J.C., (2002). Calcium Phosphate Biominerals. In M.J. Kohn, J. Rakovan, and J.M. Hughes, Eds. Phosphates: geochemical, geobiological, and materials importance, 48, p. 427-453. Reviews in Mineralogy & Geochemistry.

Frushour, B.G. and Koenig, J.L., (1975). Raman scattering of collagen, gelatin, and elastin. *Biopolymers*, 14, 379-391.

George, A. and Veis, A., (2008). Phosphorylated proteins and control over apatite nucleation, crystal growth, and inhibition. *Chemical Review*, 108 (11), 4670-4693.

Glimcher, M.J., (2006). Bone: nature of calcium phosphate crystals and cellular, structural, and physical chemical mechanisms in their formation. *Reviews in Mineralogy & Geochemistry,* 64, 223-282.

Gullekson, C., Lucas, L., Hewitt, K., and Kreplak, L. (2011). Surface-sensitive Raman spectroscopy of collagen I fibrils. *Biophysical journal*, 100 (7), 1837–45.

Hasharoni, A., Zilberman, Y., Turgeman, G., Helm, G.A., Liebergali, M., and Gazit, D., (2005). Murine spinal fusion induced by engineered mesenchymal stem cells that conditionally express bone morphogenetic protein-2. *Journal of Neurosurgery: Spine,* 3, 47-52.

Inzana, J.A., Maher, J. R., Takahata, M., Schwarz, E.M., Berger, A.J., and Awad, H.A. (2013). Bone fragility beyond strength and mineral density: Raman spectroscopy predicts femoral fracture toughness in a murine model of rheumatoid arthritis. *Journal of biomechanics,* 46(4), 723–30.

Ivanova, T.I., Frank-Kamenetskaya, O.V., Kol'tsov, A.B., and Ugolkov, V.L., (2001). Crystal structure of calcium-deficient carbonated hydroxyapatite thermal decomposition. *Journal of Solid State Chemistry,* 160, 340-349.

Karampas, I.A., Orkoula, M.G., and Kontoyannis, C.G., (2012). A quantitative bioapatite/collagen calibration method using Raman spectroscopy of bone. *Journal of Biophotonics*, 1-15.

Kazanci, M., Fratzl, P., Klaushofer, K., and Paschalis, E.P., (2006). Complementary information on *in vitro* conversion of amporphous (precursor) calcium phosphate to hydroxylapatite from Raman microspectroscopy and wide-angle x-ray scattering. *Calcified Tissue International,* 79, 354-359.

Klein, C. and Dutrow, B. (2007). Mineral Science, 23rd ed. Wiley, Hoboken.

Koljenović, S., Bakker Schut, T.C., Wolthuis, R., de Jong, B., Santos, L., Caspers, P.J., Kros, J.M., and Puppels, G. J. (2005). Tissue characterization using high wave number Raman spectroscopy. *Journal of biomedical optics,* 10(3), 031116-1-11.

Launey, M.E., Buehler, M.J., and Ritchie, R.O. (2010). On the Mechanistic Origins of Toughness in Bone. Annual Review of Materials Research, 40, 25–53.

Legros, R., Blamain, N., and Bonel, G. (1987) Age-related changes in mineral of rat and bovine cortical bone. *Calcified Tissue International* , 41, 137-144.

Lowery, J.W., Pazin, D., Intini, G., Kokabu, S., Chappuis, V., Capelo, L., and Rosen, V., (2011). The role of BMP2 signaling in the skeleton, 21(2), 177-185.

Mahamid, J., Aichmayer, B., Shimoni, E., Ziblat, R., Li, C., Siegel, S., Paris, O., Fratzl, P., Weiner, S., and Addadi, L., (2010). Mapping amorphous calcium phosphate transformation

into crystalline mineral from the cell to the bone in zebrafish fin rays. *Proceedings of the National Academy of Sciences*, 107(14), 6316-6321.

Marieb, E.N., (1997). Essentials of Human Anatomy and Physiology, 5th ed., p. 114-120. Benjamin Cummings, San Francisco.

Mi, M., Jin, H., Wang, B., Yukata, K., Sheu, T.-J., Ke, Q. H., Tong, P., Im, H-J., Xiao, G., and Chen, D. (2013). Chondrocyte BMP2 signaling plays an essential role in bone fracture healing. *Gene*, 512(2), 211–8.

Murakami, N., Saito, N., Horiuchi, H., Okada, T., Nozaki, K., and Takaoka, K., (2002). Repair of segmental defects in rabbit humeri with titanium fiber mesh cylinders containing recombinant human bone morphogenetic protein-2 (rhBMP-2) and a synthetic polymer. *Journal of Biomedical Materials Research*, 62(2), 169-174.

Nagy, A. (2000). Cre Recombinase: The Universal Reagent for Genome Tailoring. *Genesis*, 26, 99-109.

Nalla, R.K., Kruzic, J.J., Kinney, J.H., Balooch, M., Ager, J.W., and Ritchie, R.O. (2006). Role of microstructure in the aging-related deterioration of the toughness of human cortical bone. *Materials Science and Engineering: C*, 26(8), 1251–1260.

Nelson, D.G.A., and Williamson, B.E. (1982). Low-temperature laser Raman spectroscopy of synthetic carbonated apatites and dental enamel, *Australian Journal of Chemistry*, 35(4), 715-727.

Nudelman, F., Pieterse, K., George, A., Bomans, P.H.H., Friedrich, H., Brylka, L.J., Hilbers, P.A.J., de With, G., and Sommerdijk, N.A.J.M. (2010). The role of collagen in bone apatite formation in the presence of hydroxyapatite nucleation inhibitors. *Nature materials*, 9(12), 1004–9.

Orgel, J.P.R.O, Irving, T.C., Miller, A., and Wess, T.J., (2006). Microfibrillar structure of type 1 collagen *in situ*. *Proceedings of the National Academy of Sciences*, 103(24), 9001-9005.

Paschalis, E.P. , Shane, E., Lyritis, G., Skarantavos, G., Mendelsohn, R., and Boskey, A.L. (2004). Bone fragility and collagen cross-links. *Journal of bone and mineral research: the official journal of the American Society for Bone and Mineral Research*, 19(12), 2000–4.

Paschalis, E.P., Verdelis, K., Doty, S.B., Boskey, A.L., Mendelsohn, R., and Yamauchi, M. (2001). Spectroscopic characterization of collagen cross-links in bone. *Journal of bone and mineral research: the official journal of the American Society for Bone and Mineral Research*, 16(10), 1821–8.

Pasteris, J.D., (1998). In M.A. McKibben, W.C. Shanks, and W.I. Ridley, eds. Applications of microanalytical techniques to understanding mineralizing processes, p. 233-238. Society of Economic Geologists, Little, CO.

Pasteris, J.D., Wopenka, B., and Valsami-Jones, E. (2008). Bone and tooth mineralization: why apatite? *Elements*, 4(2), 97–104.

Penel, G., Leroy, G., Rey, C., and Bres, E. (1998). MicroRaman spectral study of the PO_4 and CO_3 vibrational modes in synthetic and biological apatites. *Calcified tissue international*, 63(6), 475–81.

Rogers, K.D. and Zioupos, P., (1999). The bone tissue of the rostrum of a *Mesoplodon Densirostris* whale: a mammalian biomineral demonstrating extreme texture. *Journal of Materials Science Letters*, 18, 651-654.

Saito, M., and Marumo, K. (2010). Collagen cross-links as a determinant of bone quality: a possible explanation for bone fragility in aging, osteoporosis, and diabetes mellitus. *Osteoporosis international*, 21(2), 195–214.

Seeherman, H.J., Bouxsein M., Kim, H., Li, R., Li, X.J., Aiolova, M., and Wozney, J.M., (2004). Recombinant human bone morphogenetic protein-2 delivered in an injectable calcium, phosphate accelerates osteotomy-site healing in a nonhuman primate model, *The Journal of Bone and Joint Surgery*, 86A(9), 1961-1971.

Schwartz, A.G., Lipner, J. H., Pasteris, J. D., Genin, G. M., and Thomopoulos, S. (2013). Muscle loading is necessary for the formation of a functional tendon enthesis. *Bone*, *55*(1), 44–51.

Schwartz, A. G., Pasteris, J. D., Genin, G. M., Daulton, T. L., and Thomopoulos, S. (2012). Mineral distributions at the developing tendon enthesis. *PloS one*, *7*(11), e4863

Skinner, H.C.W., (2005). Biominerals. *Mineralogical Magazine*, 69(5), 621-641.

Teitelbaum, S.L., (2000). Bone absorption by osteoclasts. *Science*, 289, 1504-1508.

Tong, W., Glimcher, M.J., Katz, J.L., Kuhn, L., and Eppell, S.J., (2003). Size and shape of mineralites in young bovine bone measured by atomic force microscopy. *Calcified Tissue International*, 72, 592-598.

Tsuji, K., Bandyopadhyay, A., Harfe, B.D., Cox, K., Kakar, S., Gerstenfeld, L., Einhorn, T., Tabin, C.J., and Rosen, V., (2006). BMP2 activity, although dispensable for bone formation is required for the initiation of fracture healing. *Nature Genetics*, 38(12), 1424-1428.

Turgeman, G., Zilberman, Y., Zhou, S., Kelly P., Moutsatsos, I.K., Kharode, Y.P., Borella, L.E., Bex, F.J., Komm, B.S., Bodine, P.V.N., and Gazit, D., (2002). Systemically administered rhBMP-2 promotes MSC activity and reverses bone and cartilage loss in osteopenic mice. *Journal of Cellular Biochemistry*, 86, 461-474.

Walton, A.G., Deveney, M.J., and Koenig, J.L., (1970). Raman spectroscopy of calcified tissue. *Calcified Tissue Research*, 6, 162-167.

Wang, L., Su, Y.-X., Zheng, G.-S., Liao, G.-Q., and Zhang, W.-H. (2013). Healing masseter entheses of mandibular reconstruction with autograft-Raman spectroscopic and histological study. *International journal of oral and maxillofacial surgery*, *42*(7), 915–22.

Wenk, H.R. and Bulakh, A., (2004). Minerals: their constitution and origin, p. 234-238. Cambridge University Press, Cambridge, UK.

Wohl, G.R., Towler, D.A., and Silva M.J. (2009). Stress fracture healing: fatigue loading of the rat ulna induces upregulation in expression of osteogenic and angiogenic genes that mimic the intramembraous portion of fracture repair. *Bone*, 44 (2), 320-330.

Wopenka, B., Kent, A., Pasteris, J.D., Yoon, Y., and Thomopoulos, S. (2008). The tendon-to-bone transition of the rotator cuff : a preliminary Raman spectroscopic study documenting the gradual mineralization across the insertion in rat tissue samples, *Applied Spectroscopy*, 62(12), 1285–1294.

Wopenka, B., and Pasteris, J.D. (2005). A mineralogical perspective on the apatite in bone. *Materials Science and Engineering: C*, *25*(2), 131–143.

Yamauchi, M., and Katz, E.P., (1993). The Post-Translational Chemistry and Molecular Packing of Mineralizing Tendon Collagens. *Connective Tissue Research*, 29, 81-98/

Yu, L., Han, M., Yan, M., Lee, J., and Muneoka, K. (2012). BMP2 induces segment-specific skeletal regeneration from digit and limb amputations by establishing a new endochondral ossification center. *Developmental biology*, *372*(2), 263–73.

Yu, Y.Y., Lieu, S., Lu, C., and Colnot, C. (2010). Bone morphogenetic protein 2 stimulates endochondral ossification by regulating periosteal cell fate during bone repair. *Bone*, *47*(1), 65–73.